Ultrasmall Amorphous Zirconia Nanoparticles Catalyze Carbon-Carbon Bond Hydrogenolysis

Shaojiang Chen,[1,12] Akalanka Tennakoon,[1,2,12] Kyung-Eun You,[3,12] Alexander L. Paterson,[1] Ryan Yappert,[4] Selim Alayoglu,[5] Lingzhe Fang,[6] Xun Wu,[1,2] Tommy Yunpu Zhao,[7] Michelle P. Lapak,[7] Mukunth Saravanan,[1] Ryan A. Hackler,[8] Yi-Yu Wang,[1,2] Long Qi,[1] Massimiliano Delferro,[8,9] Tao Li,[6,10] Byeongdu Lee,[10] Baron Peters,[4] Kenneth R. Poeppelmeier,[11] Salai C. Ammal,[3] Clifford R. Bowers,[7] Frédéric A. Perras,[1] Andreas Heyden,[3,***] Aaron D. Sadow,[1,2,**] Wenyu Huang[1,2,*]

[1] US DOE, Ames Laboratory, Iowa State University, Ames, IA, USA
[2] Department of Chemistry, Iowa State University, Ames, IA, USA
[3] Department of Chemical Engineering, University of South Carolina, Columbia, SC, USA
[4] Department of Chemical and Biomolecular Engineering, University of Illinois at Urbana-Champaign, Urbana, IL 61801, USA
[5] Center for Catalysis and Surface Science, Northwestern University, Evanston, Illinois 60208, USA
[6] Department of Chemistry and Biochemistry, Northern Illinois University, DeKalb, IL 60115, USA
[7] Department of Chemistry and National High Magnetic Field Laboratory, University of Florida, Gainesville, FL 32611, USA
[8] Chemical Sciences and Engineering Division, Argonne National Laboratory, Lemont, IL, USA
[9] Pritzker School of Molecular Engineering, University of Chicago, Chicago, IL 60637, USA
[10] X-ray Science Division, Argonne National Laboratory, Lemont, IL, USA
[11] Department of Chemistry, Northwestern University, Evanston, Illinois 60208, USA

[12] These authors contributed equally
*Correspondence: whuang@iastate.edu
**Correspondence: sadow@iastate.edu
***Correspondence: heyden@cec.sc.edu

Abstract

Zirconia, an earth-abundant, non-reducible, metal oxide, was discovered to catalyze the hydrogenolysis of aliphatic hydrocarbon polymers with activity rivaling that of precious metal nanoparticles. To achieve this unusual reactivity, a catalytic architecture was designed and constructed to localize ultrasmall amorphous zirconia nanoparticles within the nano-volume void between two fused platelets of mesoporous silica. The amorphous zirconia nanoparticles were also chemically embedded in the walls of the porous silica and protected from sintering or crystallization. Large macromolecules translocate from melted bulk polymer through radial mesopores to the highly active zirconia particles at the center of the structure to undergo selective carbon-carbon bond hydrogenolytic cleavage into a narrow, C_{18}-centered distribution. Calculations indicated that heterolytic C–H bond cleavage across a Zr–O bond of a $Zr(O)_2$ adatom model for unsaturated surface sites in the amorphous material gives a zirconium-hydrocarbyl, which is followed by C–C bond cleavage by β-alkyl elimination.

Introduction

Metal oxides are ubiquitous in catalysis as supports for active species or as catalysts themselves. Active oxides, such as those of molybdenum, tungsten, or rhenium, can react with unsaturated hydrocarbons *in situ* to generate surface alkylidene ($M{=}CR_2$) sites for olefin metathesis.[1,2] In contrast, the robust metal oxygen bonds of non-reducible oxides are used to create 3D architectures, such as in zeolites and mesoporous materials. In catalytic reactions, such materials either make use of acidic or basic surface sites or act as supports for reduced metal nanoparticles, single-atom catalysts,[3] or surface organometallic chemistry (SOMC) species, rather than forming metal-carbon bonds themselves. In principle, *in situ* conversion of non-reducible metal oxides into metal-hydride and metal-alkyl species, especially in materials with co-localized surface acid sites, could lead to unique multifunctional reaction mechanisms. Such organometalloxide catalysts could be particularly interesting for the selective cleavage of carbon-carbon bonds in hydrocarbons, which has traditionally relied on precious metal catalyzed hydrogenolysis[4-8] or acid-catalyzed hydrocracking.[9,10] Moreover, developing new processes for conversions of hydrocarbon plastics, which are currently used and discarded on a hundreds of megatons scale,[11] would also benefit from earth abundant oxide-based catalysts.

The growing global plastic waste crisis[12-14] has motivated recent studies of supported precious metal nanoparticles as catalysts for hydrogenolysis of polyolefins.[15-21] Carbon-carbon bond cleavage via organozirconium-mediated β-alkyl elimination[22] has received less attention, despite attractive mild conditions (< 150 °C, atmospheric pressure) and earth abundance of Zr.[23,24] The combination of a few of the advantageous features of these distinct classes of catalysts may provide an appropriate strategy for designing organozirconia-mediated hydrogenolysis of hydrocarbons.

The conventional strategy to achieve high activity, involving evenly dispersed sites over high surface area materials, has not yet enabled the activation of metal oxides for hydrogenolysis. An alternative catalyst design instead positions active sites at specific isolated locations within a 3D nanosized architecture. In support of this idea, a mesoporous silica shell/platinum catalyst/silica core ($mSiO_2/Pt/SiO_2$) 3D architecture that isolates small Pt nanoparticles at the bottom of mesoporous wells provides high activity and long catalyst lifetimes in polyolefin hydrogenolysis.[25,26] In contrast, external-facing platinum in Pt/SiO_2 materials readily deactivate by leaching and sintering. The synthetic methods that localize metal nanoparticles in a 3D architecture,[27,28] however, are not readily adapted to SOMC zirconium complexes due to their unwanted reactivity with air and moisture, which forces the final synthetic step to be organometallic site installation. In that covalent grafting reaction, the placement of sites is governed by the locations of surface hydroxy groups, which are notoriously difficult to control on metal oxide surfaces.[29,30] Instead, we sought to advance the construction of mixed metal oxide-silica architectures by localizing zirconia particles in a narrow zone within mesoporous silica nanoparticles.

Metal nanoparticle and SOMC catalysts both benefit from coordinatively unsaturated sites, achieved in the former through high proportions of edge and corner atoms in small nanoparticles and in the latter by immobilization onto inert supports. Although zirconia-catalyzed polyolefin hydrogenolysis had not previously been demonstrated, zirconia was shown to catalyze the hydrogenation of alkenes,[31] and hexane is cracked over zirconia to give similar products and selectivity as the HZSM-5 acid catalyst.[32] Moreover, tests of zirconia as a support for noble metals in hydrogenolysis also suggested its possible activity.[33] Smaller nanoparticles,[34] the presence of oxygen vacancies,[32] and undercoordinated sites[35] also have been proposed to enhance the reactivity

of zirconia by creating either reducible surface sites or Lewis acid sites.[36] Thus, metal oxides with coordinatively unsaturated surface sites in small nanoparticles that are isolated and stabilized by an inert 3D architecture could be promising for carbon-carbon bond hydrogenolysis.

Herein, we demonstrate that ultrasmall amorphous zirconia nanoparticles, covalently embedded in silica and localized in a void between two mesoporous platelets (L-ZrO_2@$mSiO_2$), are highly active in the hydrogenolysis of polyethylene. The architecture enhances the catalytic activity of zirconia to become comparable to that of Pt/C and improves its selectivity toward liquid products. Spectroscopic and computational studies implicate heterolytic H–H and C–H bond cleavage steps that generate Zr–H, Zr–C, and O–H bonds, indicating that organometallic elementary steps are involved in polymer deconstruction and product formation. From a practical perspective, the catalyst can be handled under ambient conditions and provides a competitive, earth-abundant, and low-cost alternative to precious metal hydrogenolysis catalysts for polyolefin deconstruction.

Results

Synthesis and Catalyst Structure. L-ZrO_2@$mSiO_2$ was designed for zirconium-catalyzed polyolefin deconstruction (Figures 1 and 2). Ultrasmall $ZrO_x(OH)_{4-2x}$ nanoparticles were dispersed on graphene oxide (GO) sheets (Figure S1), $mSiO_2$ layers were grown on the $ZrO_x(OH)_{4-2x}$/GO, and the resulting material was washed and calcined to remove structure-directing agents. Inductively coupled plasma mass spectrometry (ICP-MS) analysis of L-ZrO_2@$mSiO_2$ revealed a ZrO_2 loading of 4.7 wt.% (Table S1). ICP-MS analyses of three batches of as-synthesized L-ZrO_2@$mSiO_2$ catalysts (Table S2) ruled out the presence of any other transition metals in the catalyst, including Ru, Rh, Pt, Pd, Au, Re, Os, Ir, Ni, Fe, Co, Cu, Zn, Mo, W, Cd, Ce, Hf, Ti and V. The elemental purity of L-ZrO_2@$mSiO_2$ is further supported by X-ray photoelectron spectroscopy (XPS) (Figure S2) and energy dispersive X-ray spectroscopy (EDX; Figure S3).

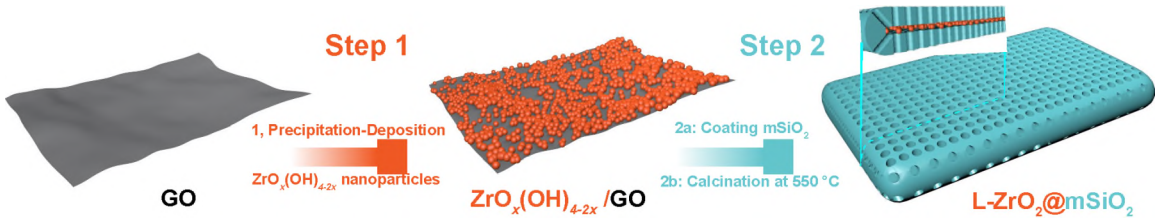

Figure 1. Construction of L-ZrO_2@$mSiO_2$. Step 1: precipitation-deposition of $ZrO_2(OH)_{4-2x}$ nanoparticles onto GO. Step 2a: coating $mSiO_2$ onto $ZrO_2(OH)_{4-2x}$/GO. Step 2b: calcination at 550 °C.

The performance of L-ZrO_2@SiO_2 is best understood through comparisons to the behavior of several reference catalysts, whose relevant structures are briefly described here and summarized in Table S1. $mSiO_2$, synthesized by templated silica growth on GO,[37,38] has the same layered platelet morphology and porous structure (Figure S4) as L-ZrO_2@$mSiO_2$. imp-ZrO_2/$mSiO_2$, produced by incipient wetness impregnation of zirconium precursors into $mSiO_2$, contains randomly dispersed amorphous ZrO_2 nanoparticles (Figure S5). ZrO_2-6/$mSiO_2$ was prepared by immobilizing pre-synthesized 6 nm monoclinic ZrO_2 nanoparticles (Figure S6) on the external surface of $mSiO_2$ (Figure S7). ZrO_2-30 and Pt/C are commercial monoclinic ~30 nm-sized zirconia and 1.3 ± 0.4 nm-sized platinum nanoparticles supported on carbon (Figure S8), respectively. L-Pt@$mSiO_2$ (Figure S9), synthesized by deposition of $PtO_x(OH)_{4-2x}$ nanoparticles on GO (Figure S10) followed by growth of the $mSiO_2$ shell, creates a comparable architecture to L-ZrO_2@$mSiO_2$

with 3.5 ± 0.8 nm platinum nanoparticles instead of zirconia. The total surface area and Barrett-Joyner-Halenda (BJH) pore size for $mSiO_2$-based samples are ~900-1000 m^2/g and 3.4 – 3.8 nm, respectively (Table S1).

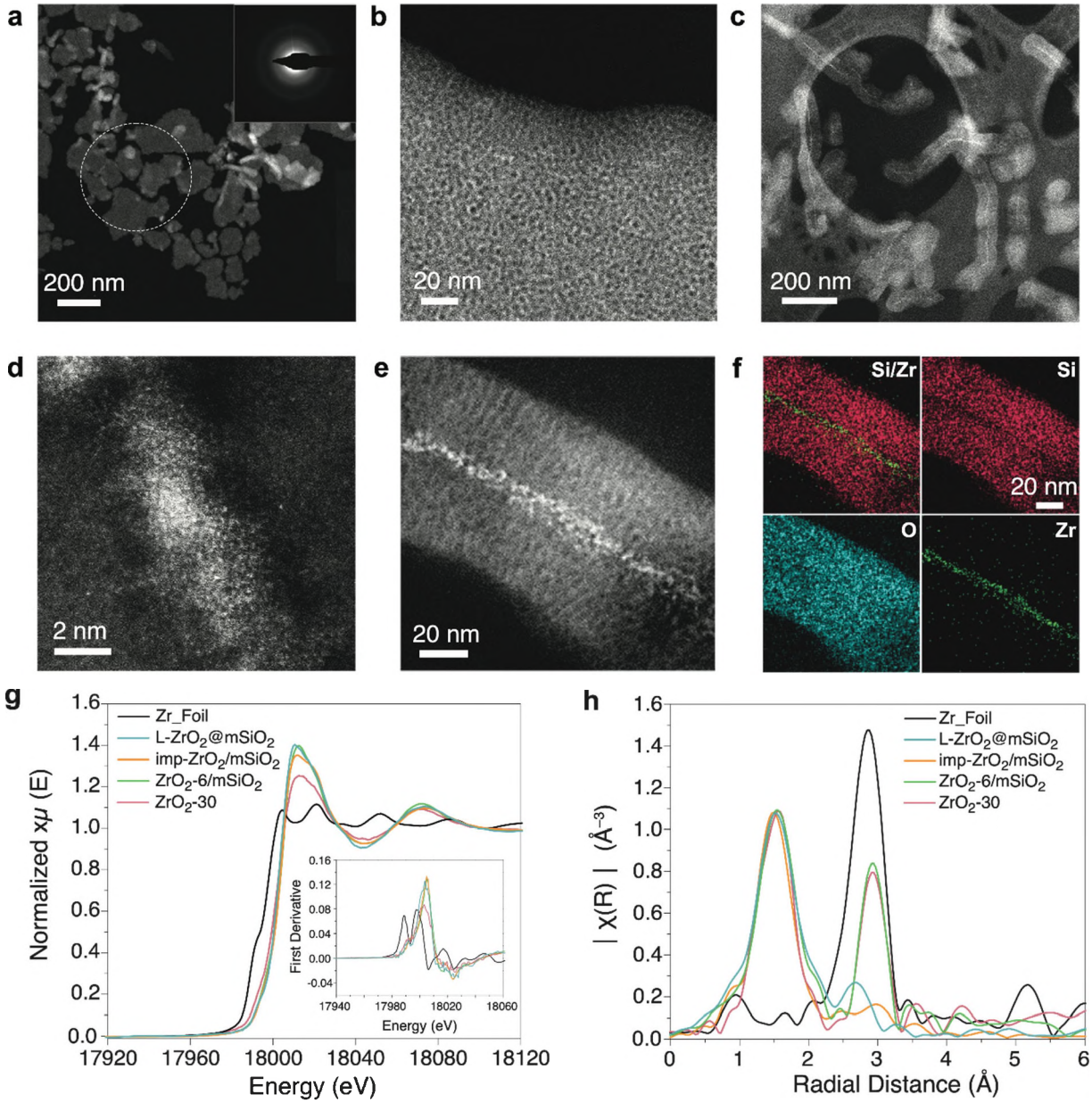

Figure 2. a) Low-magnification (inset: SAED pattern) and b) high-magnification high-angle annular dark-field (HAADF) scanning transmission electron microscopy (STEM) images of L-ZrO_2@$mSiO_2$. c) Low-magnification and d) high-resolution HAADF STEM image of the cross-section of a L-ZrO_2@$mSiO_2$ particle prepared by microtome. e) High-magnification HAADF STEM image and f) the corresponding EDX elemental (Si and Zr; Si; O; Zr) maps of the cross-section of a L-ZrO_2@$mSiO_2$ particle. g) Normalized Zr K-edge XANES spectra (inset: first derivative spectra) and h) k_2-weighted FT-EXAFS spectra of L-ZrO_2@$mSiO_2$ and control samples.

The low magnification scanning transmission electron microscopy (STEM) image (Figure 2a) of L-ZrO_2@mSiO_2 showed its separated nanoplatelet particle morphology, with lateral dimensions ranging from hundreds of nanometers to a few microns. Pore diameters of 3.4 ± 0.4 nm in the mesoporous silica nanoplatelets, revealed by the higher magnification image (Figure 2b), matched the values obtained with N_2 sorption isotherm measurements (Table S1, Figure S11). Notably, the STEM images of cross-sectioned L-ZrO_2@mSiO_2 particles prepared by ultramicrotome (Figure 2c-e) clearly showed a thin (~3 nm) bright band, identified by elemental mapping as a region of concentrated zirconium (Figure 2f), between the two 35 nm-thick sheets of mSiO_2. The mesopores in mSiO_2 are aligned perpendicular to the nanoplate (Figure 2e),[38,39] and the diameter of the ZrO_2 particles is 3.0 ± 0.5 nm (Figure S12).

The amorphous nature and chemical structure of the ultrasmall ZrO_2 nanoparticles in L-ZrO_2@mSiO_2 were established by electron diffraction, powder X-ray diffraction (pXRD), X-ray absorption spectroscopy (XAS), and solid-state nuclear magnetic resonance (SSNMR) spectroscopy. A diffuse ring in the selected-area-electron diffraction (SAED) pattern (inset in Figure 2a) indicated amorphous characteristics of the material, in contrast to sharp diffraction spots or rings typical of crystalline substances.[40] The high-resolution image (Figure 2d) further revealed that both ZrO_2 and mSiO_2 lack long-range order. Diffraction peaks from ZrO_2 were not detected in the pXRD pattern of L-ZrO_2@mSiO_2 (Figure S13). The strong pre-edge peak in X-ray absorption near-edge structure (XANES) spectra (Figure 2g) and the same peak intensity in Fourier Transformed extended X-ray absorption fine structure (EXAFS) spectra (Figure 2h) for the Zr-O distance in all ZrO_2 samples confirmed that Zr is in +4 oxidation state.[41,42] The non-crystalline nature of ZrO_2 in L-ZrO_2@mSiO_2 was distinguished by EXAFS from crystalline ZrO_2-6/mSiO_2 and ZrO_2-30, which contained a Zr–Zr scattering path at 2.9 Å.

The direct (e→^{17}O) dynamic nuclear polarization (DNP) surface-enhanced (SENS)[43,44] magic angle spinning (MAS) ^{17}O Hahn echo NMR spectrum of L-ZrO_2@mSiO_2 (Figure 3a) contained a broadened, axially-symmetric, quadrupolar powder pattern with an isotropic chemical shift of 50 ppm and a quadrupolar coupling constant of 5 MHz, assigned to siloxane linkages. To aid in the assignment of additional broad signals at 400 and 150 ppm at 9.4 T, likely attributable to the ZrO_2 nanoparticles, we acquired DNP SENS data on pure monoclinic ZrO_2 nanoparticles (Figure 3b). ZrO_2-30 gave rise to sharp resonances at 325 ppm and 402 ppm from μ^4-O^{2-} and μ^3-O^{2-} lattice sites[45] and a broad resonance from approximately 425-300 ppm from surface μ^3- and μ^4-O^{2-} sites. The resonance at 400 ppm in the ^{17}O Hahn echo spectrum of L-ZrO_2@mSiO_2 was assigned to disordered surface Zr oxide sites. In addition, the sharp signals from the crystalline ZrO_2 phase contrasted the broad resonances from L-ZrO_2@mSiO_2, further supporting the conclusion that the ZrO_2 particles are amorphous. We further performed indirect (e→^{1}H→^{17}O) DNP SENS experiments to assign the resonance at 150 ppm in L-ZrO_2@mSiO_2, using phase-shifted recoupling effects a smooth transfer of order (PRESTO) experiments to acquire the ^{17}O MAS NMR spectra of only the hydroxy species.[46-48] The PRESTO spectrum of L-ZrO_2@mSiO_2 (Figure 3c) was dominated by a previously-obscured resonance at approximately –50 ppm assigned to surface silanols. Alternatively, the spectrum of ZrO_2-30 contained a signal at approximately 150 ppm at 9.4 T (Figure 3d), unambiguously assigned to Zr–OH sites.[45,49] The contrast between the spectra of the two samples suggests that a dominant component of the resonance at 150 ppm in the ^{17}O Hahn echo spectrum of L-ZrO_2@mSiO_2 is not a Zr–OH species but rather Si–O–Zr linkages. We observed such a site in a previous study of a $Zr(NMe_2)_3$/SiO_2 species where it resonated at 146 ppm at 9.4 T.[50] Importantly, the observation of this resonance confirms that the silica and zirconia phases are covalently linked to one another.

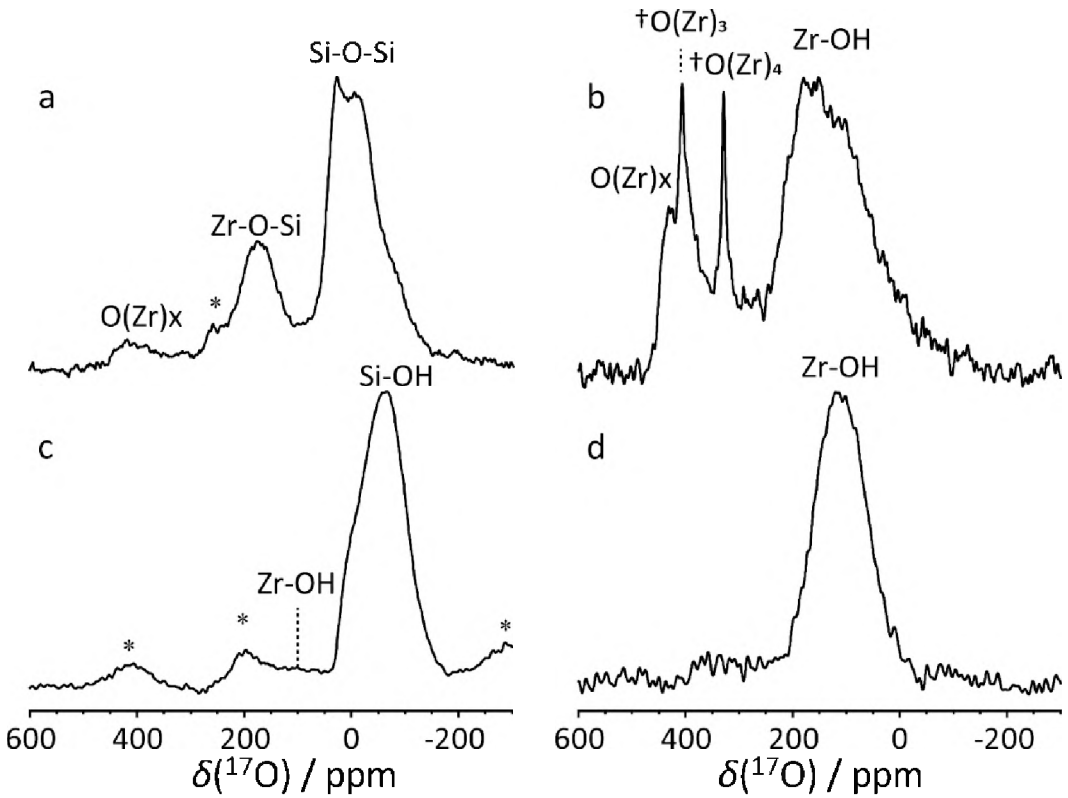

Figure 3. Direct DNP-enhanced ^{17}O Hahn echo spectra of a) L-ZrO_2@mSiO_2 and b) monoclinic ZrO_2-30 nanoparticles. Indirect DNP-enhanced $^{17}O\{^1H\}$ PRESTO NMR spectra of c) L-ZrO_2@mSiO_2 and d) ZrO_2-30 nanoparticles. All data were acquired at a MAS rate of 14 kHz. Spinning sidebands are indicated by asterisks. Crystalline sites are further labeled using a dagger.

The thermochemical stability of ZrO_2 is affected by the mSiO_2 shell. Calcination of $ZrO_x(OH)_{4-2x}$/GO at 550 °C formed a mixture of tetragonal and monoclinic ZrO_2 nanocrystals (Scherrer size 5.5 and 9.3 nm, respectively; Figure S14). Similar calcination of L-ZrO_2@mSiO_2 did not provide detectable signals of crystalline domains (Figure S13). Likely, the confinement of ultrasmall ZrO_2 nanoparticles within the mesopores, along with the covalent Si-O-Zr bonding, limits their growth and crystallization.

Polymer Deconstruction Catalysis. Polyethylene (PE) hydrogenolysis was performed with ~3 g of melted PE (M_n = 20 kDa, M_w = 91 kDa, Figure S16) and 5.5 mg of catalyst under 0.992 MPa of H_2 at 300 °C as the standard conditions. The high mass specific catalytic activity of L-ZrO_2@mSiO_2 was established by the rate of C–C bonds cleaved per metal mass (2.3 ± 0.4 mol $H_2 \cdot Zr\, g^{-1} \cdot h^{-1}$). The number of C–C bonds that were broken in each experiment was determined by measuring the consumption of H_2 (each H_2 molecule consumed corresponds to one hydrogenolyzed C–C bond) and by comparing starting and final total molecular weight distributions (number-averaged molecular weight, M_n) of the entire sample, including the C_1-C_9 species in the reactor headspace, the C_8-C_{50} liquid and wax fraction extracted with dichloromethane, and the $>C_{50}$ polymeric solid residue (Figure 4a,b, Tables S3 and S6). The M_n vs time curve follows the generally expected decay (Figure S15).

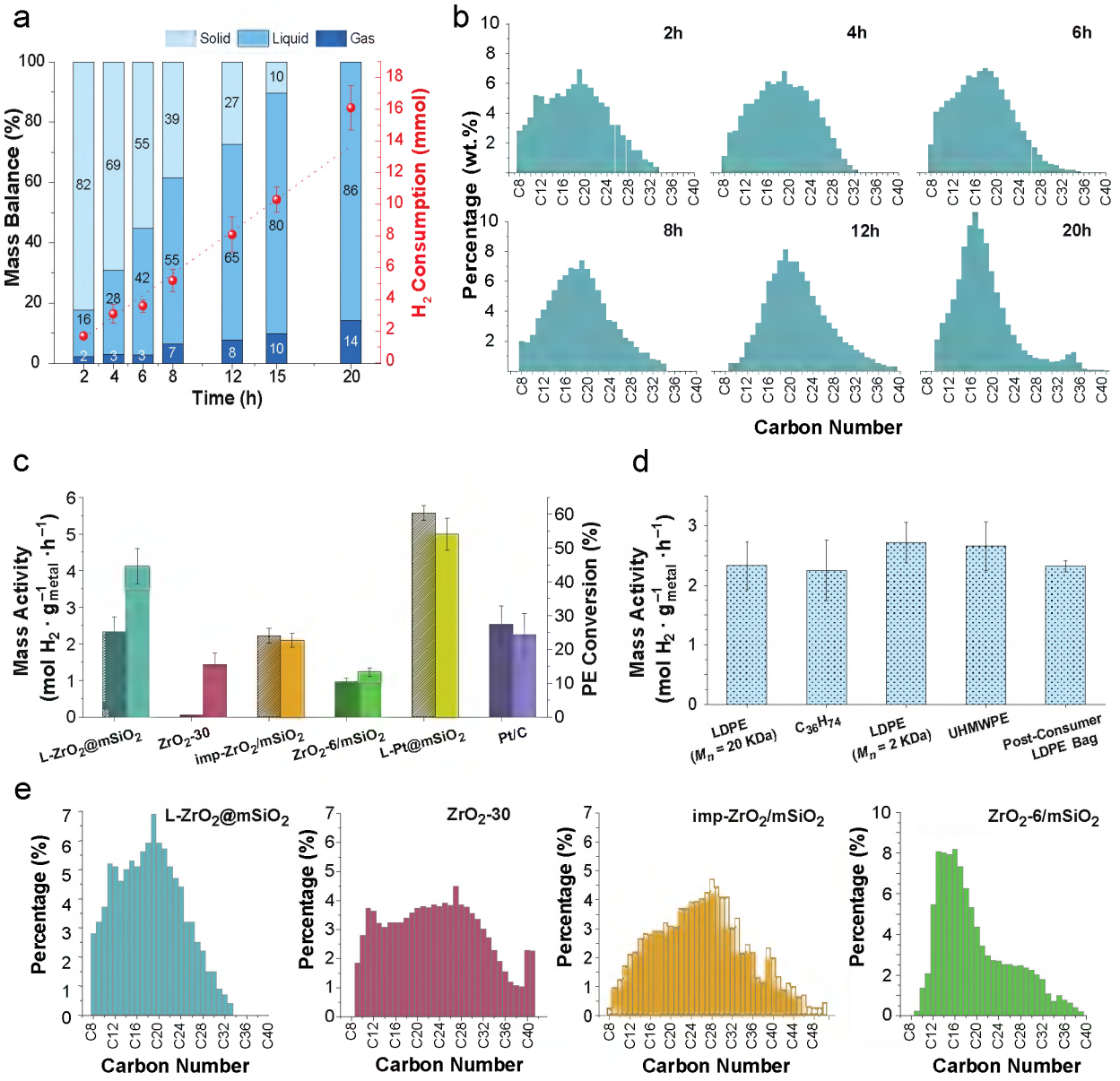

Figure 4. a) Time-dependent conversion of PE (M_n = 20 kDa, M_w = 90 kDa, $Đ$ = 4.8), liquid yield, and volatile yield in mass percentage catalyzed by L-ZrO_2@mSiO_2 under H_2 at 300 °C. b) Carbon number distribution of liquid products from hydrogenolysis of PE catalyzed by L-ZrO_2@mSiO_2 after 2, 4, 6, 8, 12, and 20 h. c) Comparison of C–C bond cleavage activity (left axis) and conversion of PE (right axis) at 300 °C for 6 h. d) Comparison of C–C bond cleavage reactivity for short and long, linear and branched polymers in L-ZrO_2@mSiO_2-catalyzed hydrogenolysis. e) Carbon number distribution of liquid products catalyzed by L-ZrO_2@mSiO_2, ZrO_2-30, imp-ZrO_2/mSiO_2, and ZrO_2-6/mSiO_2, obtained from reactions that consumed similar mols of H_2.

A few zirconia materials show catalytic activity in PE hydrogenolysis, with L-ZrO_2@mSiO_2 providing the highest conversion of PE and high mass-specific activity for C–C bond breakage (Figure 4c). Its activity for C–C bond cleavage is ca. 23±2× and 2.4±0.3× higher than the activities of ZrO_2-30 and ZrO_2-6/mSiO_2, and comparable activity to imp-ZrO_2/mSiO_2

(Table S6). Remarkably, the activity of L-ZrO_2@mSiO_2 for C–C cleavage is even competitive with that of Pt-based catalysts following the trend L-ZrO_2@mSiO_2 ~ Pt/C < L-Pt@mSiO_2. The similar activity of Pt and confined Zr, along with the <0.001 wt % concentration of other transition metals measured by ICP-MS of as-synthesized and post-reaction zirconia catalysts, as well as catalyst-free control experiments, also ruled out trace contaminants as being catalytically important species.

The L-ZrO_2@mSiO_2-catalyzed PE hydrogenolysis produced a narrow, Gaussian-type C_{18}-centered distribution of liquid hydrocarbons, with C_9-C_{27} representing >90% of the chains. This characteristic distribution was formed at the initial stage of the reaction and increased in yield in a roughly linear fashion until ca. ~75% PE conversion (Figure 4a,b and Table S3). The volatile species, which represented the low-end tail of the product distribution, similarly increased in yield as the reaction progressed (Figures S20-S44). After >80% conversion of the PE, the average chain length in the liquid products decreases to C_{16} after 15 h (Figures S47-48) and sharpens after 20 h (Figure 4b), and the weight fraction of volatile products, mostly composed of methane and ethane, further increased (Figures S45-S53). We attribute these observations to the secondary hydrogenolysis of the C_{18}-centered distribution that occurred primarily at the ends of the chains. These results further indicate that L-ZrO_2@mSiO_2-catalyzed hydrogenolysis is selective for the long hydrocarbon chains of PE rather than the shorter chains of the primary products. This remarkable behavior resembles mSiO_2/Pt/SiO_2-catalyzed hydrogenolysis of PE,[25,26] and contrasts the performance of the other ZrO_2 catalysts, which give broader, non-Gaussian or multimodal distributions (Figures 4e), which also vary throughout the PE conversion (Tables S4 and S6, Figure S54-87).

This highly disperse PE (M_n = 20 kDa) represents the typical range used for flexible packaging applications. Accordingly, L-ZrO_2@mSiO_2-catalyzed hydrogenolysis of a post-consumer LDPE grocery bag (M_n = 10.6 kDa, M_w = 150 kDa; dried under vacuum; Figure S18) resulted in equivalent reactivity (Figure 4d; 2.3 ± 0.4 mol $H_2 \cdot Zr\ g^{-1} \cdot h^{-1}$). The catalytic activity was also similar for hexatriacontane (n-$C_{36}H_{74}$), LDPE (M_n = 2.8 kDa, M_w = 5.3 kDa; Figure S17), and ultra-high molecular weight high density polyethylene (UHMW HDPE, M_w ~ 3,000-5,000 kDa). These results suggest that rates of threading of chains into pores and translocation to the active sites at the ends of the pores are not limiting the rates of C–C bond cleavage for short and long chains as well as branched and linear polymers, and the distribution is independent of C–C bond cleavage rate; however, the conformations of long and short chains likely vary to influence the distributions. Specifically, hydrogenolysis of hexatriacontane provided a distribution of chain end-cleaved hydrocarbons, similar to the process observed for secondary hydrogenolysis of C_{18} primary products noted above. On the other hand, UHMW HDPE or post-consumer LDPE gave broad distributions, respectively (Figures S88-S103). In addition, L-ZrO_2@mSiO_2 produced a narrower distribution of chain lengths of extractable species compared to the other ZrO_2-based catalysts at a similar PE conversion (39-54%, Figure 4e).

Mechanistic analysis. The amorphous ZrO_2 NPs in L-ZrO_2@mSiO_2, leading to low-coordinated metal ions,[51-55] were modeled by a Zr-adatom supported on a (–111) surface of monoclinic ZrO_2 (Zr/ZrO_2). A constrained *ab* initio thermodynamic analysis of 21 structures (Figure S106; Table S9) with varying numbers of H, O, and OH groups adsorbed on the Zr-atom identified $Zr(O)_2/ZrO_2$ as the lowest energy of a possible adatom species with reference to Zr/m-ZrO_2, gas phase H_2, and trace H_2O (a0 in Figure 5; ΔG = –3.41 eV, T = 300 °C, P_{H2} = 0.90 MPa, $P_{H2O} = 6.89 \times 10^{-15}$ MPa). In $Zr(O)_2/ZrO_2$, the Zr adatom is bonded to two oxo species with short Zr–O interatomic distances

(1.92 and 1.97 Å) and coordinated by surface oxygen donors with longer Zr–O distances. The oxo species are also bridged to the Zr of the support. The resulting electron deficient, low coordinate Zr species are representative of adatom, corner, and edge sites that are expected to be widely present in the amorphous ZrO_2 NPs. The $Zr(O)_2/ZrO_2$ species reacts with H_2 via heterolytic dissociation, leading to $HZr(OH)(O)/ZrO_2$ ($\Delta G = -3.34$ eV, b0 in Figure 5, Table S8).

This heterolytic dissociation of H_2 on L-ZrO_2@mSiO_2 was supported by *in situ* diffuse reflectance infrared Fourier transform spectroscopy (DRIFTS) experiments under flowing H_2 at 300 °C, which revealed a small peak at 1547 cm^{-1}, bands at 3731 and 1613 cm^{-1}, and a broad feature at 3600-3100 cm^{-1} (Figure S104). The signal at 1547 cm^{-1} disappeared upon flowing D_2; however, the expected band at about 1100 cm^{-1} was not detected above the strong silica absorption (Figure S105). The peak intensities at 3730 cm^{-1} and 3600-3100 cm^{-1} also diminished under D_2, and signals appeared at 2700 cm^{-1} and 2600-2300 cm^{-1}. These signals disappeared and the original features reappeared upon flowing H_2. On the basis of this H/D exchange behavior and reported assignments,[56-60] the band at 1547 cm^{-1} was assigned to ν_{ZrH} and the other signals were attributed to ν_{OH} from SiOH and ZrOH, providing experimental support for the idea of heterolytic dissociative adsorption of H_2 and D_2 in L-ZrO_2@mSiO_2.

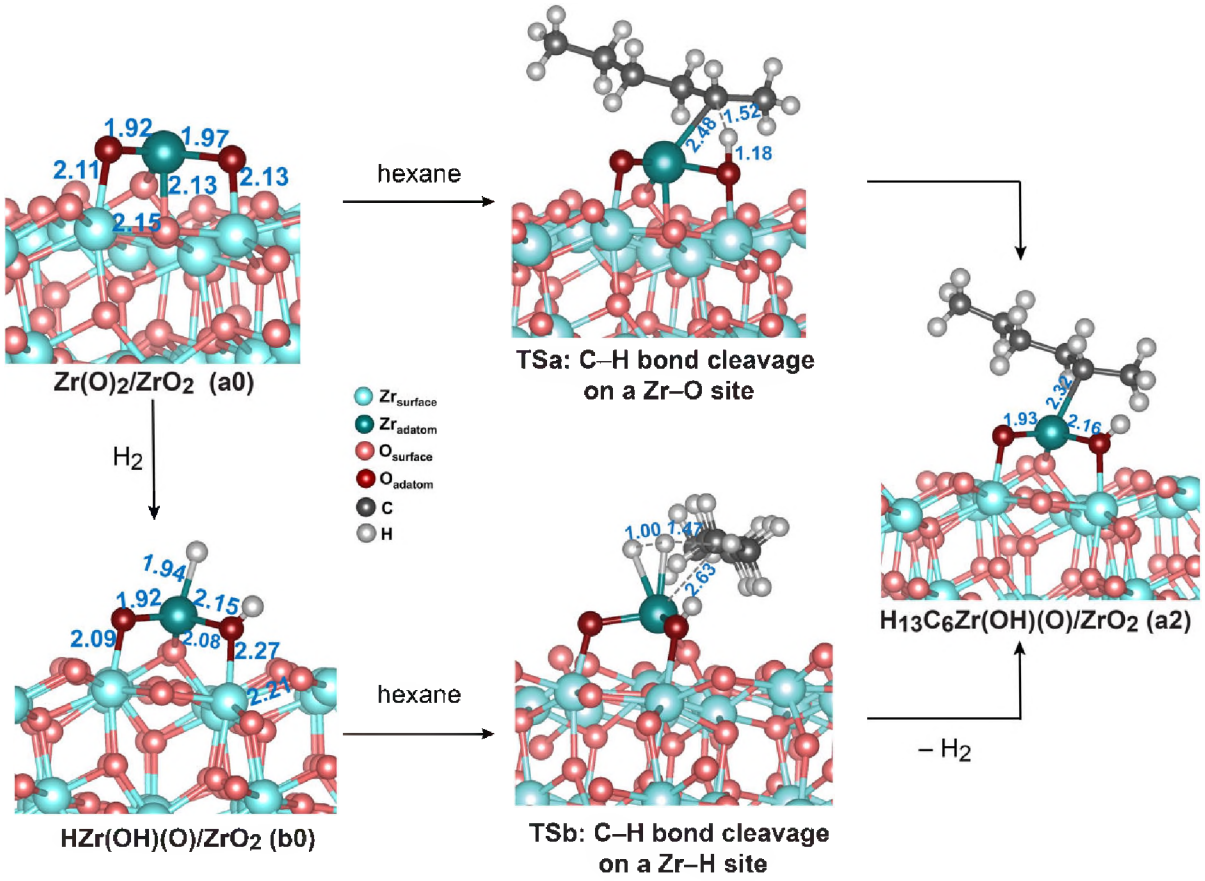

Figure 5. Side view of the optimized structures of intermediates and transition states (TS) corresponding to the initial C–H bond activation of hexane over $Zr(O)_2/ZrO_2$ (**a0**) and H–$Zr(OH)(O)/ZrO_2$ (**b0**) adatom models, both forming $H_{13}C_6Zr(OH)(O)/ZrO_2$ (**a2**). Distances are given in Å.

Low energy pathways were investigated computationally using density functional theory (DFT), and several plausible models for hydrogenolysis of n-hexane by the $Zr(O)_2/ZrO_2$ species at 300 °C under 0.1 MPa of H_2 are presented here (Figure 6). Although the experimental study focused primarily on polyethylene, the secondary cleavage of the C_{18}-centered primary products or hydrogenolysis of hexatriacontane indicates that L-ZrO_2@mSiO_2 is also a catalyst for small molecule hydrogenolysis. Hexane and the low-coordinated $Zr(O)_2$ react through an initial C–H bond activation to form $H_{13}C_6$-Zr(O)(OH)/ZrO_2 (a1→a2), involving transfer of a hexane H atom to one of the O atoms and the hexyl group to the Zr atom. This step, as well as the heterolytic H_2 cleavage above, is reminiscent of 1,2-addition of a C–H or H–H bond across a Zr=NR to give C–Zr–NHR or H–Zr–NHR.[61-64] Hexane metalation by H–Zr(OH)(O)/ZrO_2 to give $H_{13}C_6$-Zr(O)(OH)/ZrO_2 with liberation of H_2 (b1→a2), similar to the σ-bond metathesis reaction of $(SiO)_3ZrH$ and hydrocarbons,[23] is ruled out by its 0.5 eV higher barrier than that of hexane dissociative adsorption on $Zr(O)_2/ZrO_2$.

Kinetically favorable cleavage of the β-C–H bond in $H_{13}C_6$-Zr(O)(OH)/ZrO_2 produces cis-2-hexene (a2→c1, G^{act} = 0.94 eV), 1-hexene, or trans-2-hexene (via < 0.3 eV higher barrier compared to cis-2-hexene). Alternatively, the 1.26 eV barrier for β-C–C bond cleavage in $H_{13}C_6$-Zr(O)(OH)/ZrO_2 to give a3 is slightly higher. After hydrogenation of the propene product to propane, this pathway is thermodynamically more favorable than the endergonic formation of cis-2-hexene. Our calculations predicted a free energy of 1.8 eV for the C–C bond cleavage transition state (TS) over the $Zr(O)_2$ model, which is the highest energy state in the free energy profiles of $Zr(O)_2$ active site models (Figure 6). Thus, this process could be rate-limiting for n-hexane and possibly also polyethylene hydrogenolysis. In addition, C–H or C–C bond cleavage steps solely based on acidic Zr(OH) have much higher activation barriers (G^{act} = 2.05 and 2.30 eV, respectively) than 1,2-addition and β-elimination. A bona fide acid catalyst, beta zeolite, under the standard hydrogenolysis condition gave coke and branched products in experiments using PE. The differences between acid- and L-ZrO_2@mSiO_2-catalyzed deconstructions further support the organozirconia-catalyzed computational mechanism.

Propane is eliminated by a proton transfer from the proximal hydroxy to the propylzirconium species to regenerate the $Zr(O)_2$ species; the protonolytic propane elimination distinguishes this pathway from the σ-bond metathesis mechanism typically proposed for reactions of H_2 and molecular organozirconium compounds in solution. The activation barrier for an alternative mechanism involving the σ-bond metathesis-type reaction of H_7C_3–Zr(O)(OH) and H_2, as established for reactions of Cp_2ZrHR and hydrogen[65] as well as in catalytic alkene hydrogenation or alkane hydrogenolysis by seemingly related SOMC species $(\equiv SiO)_3ZrH$,[66-68] is ca. 0.4 eV higher than protonolytic elimination and appears less likely. In support of this idea, the reaction of grafted ≡Si–O–$Zr(CH_2CMe_3)_3$ and H_2 requires several hours at 150 °C.[69] Although the hydridozirconium species H–Zr(O)OH is neither involved in C–H bond metalation nor formed from H_7C_3–Zr(O)(OH) and H_2, it is nonetheless essential for hydrogenation of propene (a5 → a7).

These reaction steps were confirmed by parahydrogen induced polarization (PHIP) NMR spectroscopy, a technique that produces NMR signal enhancements only when the hydrogenation with parahydrogen occurs by pairwise addition. A PHIP signal in the ^1H PHIP NMR[70] spectrum for the L-ZrO_2@mSiO_2-catalyzed propylene hydrogenation using 99% parahydrogen (pH_2) (Figure S108) showed net alignment multiplet patterns of the CH_2 and CH_3 peaks, with integral ratios close to 1:-1. Thus, the propane product had received both protons from the same pH_2 molecule with retention of spin-spin coupling,[71,72] in accordance with the steps a5 → a7. The σ-bond metathesis reaction of H_2 and propylzirconium transfers only a single proton from a

parahydrogen molecule and cannot produce the NMR signal enhancements in accordance with the above calculations. Moreover, 1,2-addition of the hydrocarbon CH bond (e.g., a1→a2) is the reverse reaction of propane elimination, by H transfer from OH to propylzirconium (a6→a7). The principle of microscopic reversibility and the PHIP results together indicate that hydrocarbon metalation on L-ZrO_2@mSiO_2 is more consistent with 1,2-addition than dehydrogenative metalation by σ-bond metathesis, again in line with calculations.

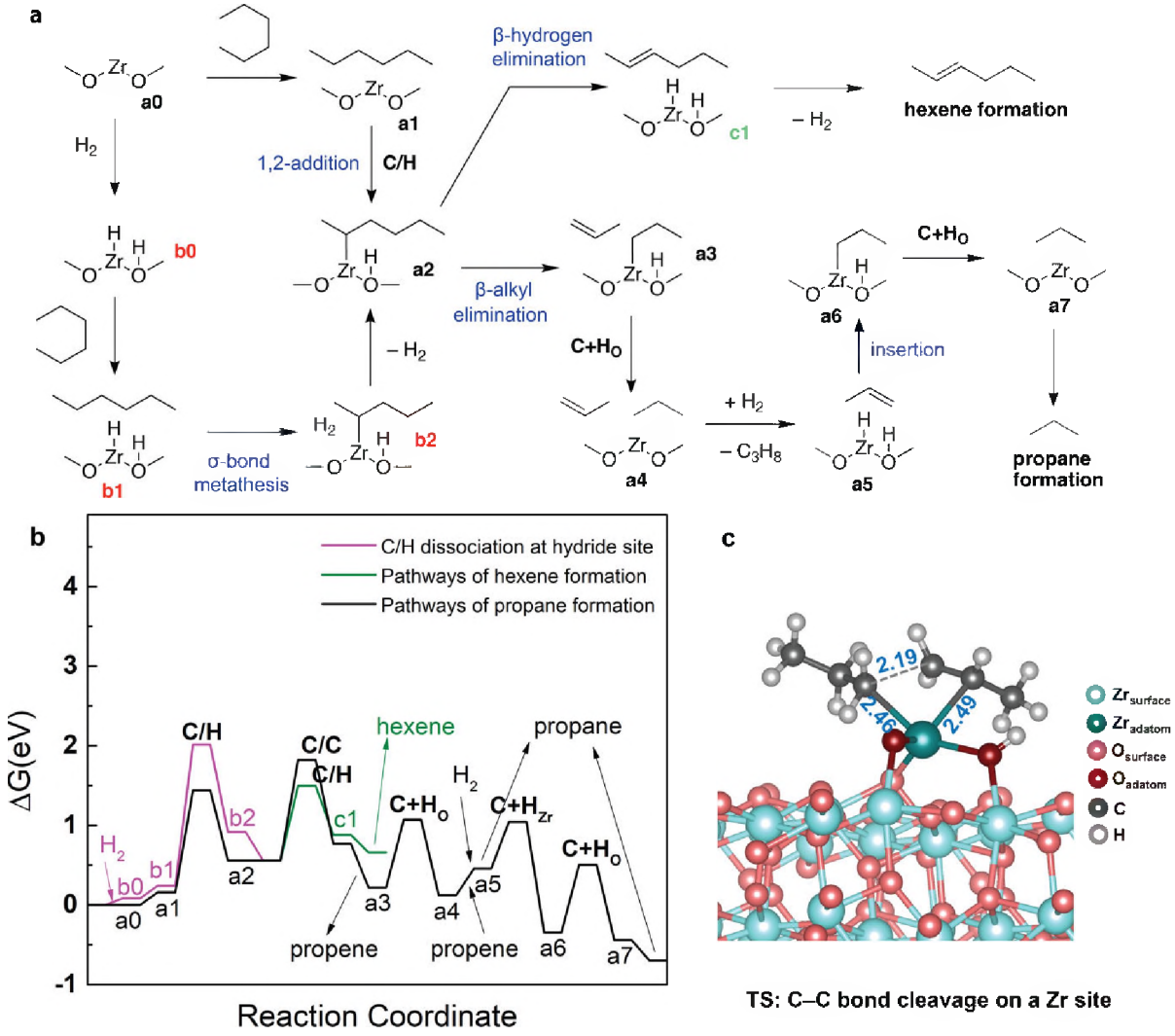

Figure 6. a) Schematic of the reaction pathways considered for n-hexane hydrogenolysis on the $Zr(O)_2$/m-ZrO_2 and H–Zr(O)(OH)/m-ZrO_2 models. b) the corresponding free energy profiles (T = 300 °C, P_{gas} = 0.1 MPa). All free energies are with reference to the sum of the energies of the $Zr(O)_2$/m-ZrO_2 catalyst model and the reactant gas molecules. c) Transition state calculated for C–C bond dissociation.

A microkinetic model was used to further examine the n-hexane hydrogenolysis over the $Zr(O)_2$/m-ZrO_2 active site, employing a continuous stirred-tank reactor (CSTR; T = 300 °C, P_{H2} = 1 MPa, P_{hexane} = 0.1 MPa, Table 1). The model revealed that as hexane conversion increases with increased residence time, selectivity for the C–C bond cleavage product, propane, increases to 100%

at sufficiently high residence times. These results suggest that the C–C bond cleavage is favored in the presence of H_2, which shifts the equilibria toward the propane formation. The microkinetic model also predicted a high steady-state surface coverage of H–Zr(O)OH ($\theta = 0.63$) under H_2 (1 MPa), which further promoted the conversion of propene to propane. Reasonable turnover frequencies, on the order of 10^{-4} s^{-1}, were observed in the microkinetic model when hexane conversion to propane was between 0.1-12.4%.

Table 1. Conversion, selectivity, and turnover frequencies of n-hexane hydrogenolysis predicted by microkinetic CSTR model for the $Zr(O)_2$/m-ZrO_2 active site with respect to the effective residence time.[a]

Effective Residence Time ($\alpha \times \tau$) [s]		**initial**	**10^{-6}**	**10^{-4}**	**10^{-2}**	**1**	**10^{2}**	**10^{4}**
Conversion (%)		-	6×10^{-6}	3×10^{-5}	1×10^{-3}	1×10^{-1}	12	94
Selectivity (%)	hexene:	100	98	42	9×10^{-1}	9×10^{-3}	9×10^{-5}	9×10^{-7}
	propane:	3×10^{-2}	2	58	99	100	100	100
	propylene:	3×10^{-2}	1×10^{-1}	4×10^{-2}	7×10^{-4}	8×10^{-6}	2×10^{-6}	1×10^{-6}
Turnover Frequency [s^{-1}]		4×10^{-1}	6×10^{-3}	2×10^{-4}	1×10^{-4}	1×10^{-4}	1×10^{-4}	9×10^{-6}

[a] (T = 300 °C, P_{H2} = 1 MPa, P_{hexane} = 0.1 MPa)

The activation barriers of H_2 dissociation and the rate-limiting C–C bond cleavage calculated from the $Zr(O)_2$/m-ZrO_2 model were compared with those from the most stable flat surfaces of monoclinic ZrO_2 (–111) and tetragonal ZrO_2 (101) surface sites (Figure S107). H_2 activation was found to be both kinetically and thermodynamically less favorable on the flat surfaces compared to the $Zr(O)_2$/m-ZrO_2 model. The C–C bond cleavage barriers on the flat surfaces are in the range of 2.1-2.4 eV, in contrast with the 1.26 eV for low-coordinated Zr sites, indicating that flat crystal surfaces of ZrO_2 are less active for breaking the C–C bonds of hydrocarbons. Thus, these results are consistent with the experimental observation that ultrasmall amorphous ZrO_2 NPs are more active in PE hydrogenolysis than larger crystalline ZrO_2 NPs dominated by more stable flat surfaces.

Conclusion

Our synthetic, spectroscopic, and mechanistic investigations of L-ZrO_2@mSiO_2 reveal the combined architectural and chemical features which enable an earth abundant, non-reducible metal oxide (Zr, Si, O) to catalyze the selective hydrogenolysis of hydrocarbon polymers. The synthesis of L-ZrO_2@mSiO_2 demonstrates, remarkably, that $ZrO_x(OH)_{4-x}$ nanoparticles are stable under the hydrolytic conditions necessary for growth of mesoporous silica and creation of the catalytic architecture with core-localized nanoparticles. Moreover, the catalytically requisite coordinatively unsaturated surface sites in amorphous zirconium are stabilized by covalently embedding the nanoparticles in the walls of mesoporous silica. These sites, modeled as $Zr(O)_2$ surface species in DFT calculations, mediate C–C bond hydrogenolysis with comparable activity to Pt/C. The quantitative comparison of activity across a series of catalysts is based on H_2 consumption or the relationship between the number of C–C bonds that are cleaved and the change in M_n of the entire hydrocarbon population, determined from the detailed characterization of gas, liquid, and solid compositions. This quantitative comparison reveals that the catalytic enhancement observed with L-ZrO_2@mSiO_2 is more than simply the combination of small crystalline ZrO_2 with mSiO_2, as shown by the poorer activity of ZrO_2-6/mSiO_2.

In addition, L-ZrO_2@$mSiO_2$ provides advantageous selectivity over the other zirconia-based catalysts investigated in this study. Alignment of long chains in the pores,[25] non-dissociative adsorption of polymer onto the walls of silica, and escape of smaller products through the void space between the two mesoporous silica plates may all contribute to higher selectivity. In fact, both L-ZrO_2@$mSiO_2$ and L-Pt@$mSiO_2$ have sites localized at the ends of mesopores and are both more selective than their non-pore-confined analogues. The mechanisms of zirconia and platinum catalyzed reactions, however, are distinct. In fact, the energetically favorable heterolytic mechanism for H–H and C–H bond cleavage on $Zr(O)_2/ZrO_2$ is different than those proposed for reducible oxides or metal nanoparticles, or even the SOMC zirconium hydride, instead resembling 1,2-addition to zirconium imido compounds. That heterolytic cleavage generates O–H and Zr–H or Zr–CH_2CH_2R species, which subsequently engage in protonolytic elimination, insertion, and β-alkyl elimination. Thus, the proposed active species is a bifunctional (hydroxy)organozirconium oxide species. Access to such species directly from ZrO_2, rather than by grafting neopentylzirconium onto silica, allows the catalytic architecture to be constructed under aqueous conditions, as well as enabling the catalytic chemistry to be accessed with air-stable precursors. In this sense, hydrogenolysis with L-ZrO_2@$mSiO_2$ is a previously unrecognized heterogeneous analogue of the SOMC-catalyzed C–C cleavage processes.

Methods

Synthesis

L-ZrO_2@$mSiO_2$. The L-ZrO_2@$mSiO_2$ sample, containing ZrO_2 nanoparticles at the interior cavity of mesoporous silica platelets, was prepared through a two-step synthesis method. In the first step, precipitated zirconium oxyhydroxide nanoparticles were deposited onto GO in an aqueous solution to give $ZrO_{2-x}(OH)_{2x}$/GO. That material was prepared as follows: Urea (0.150 g) was dissolved in DI-H_2O (100 mL), GO (10 mg) was added, and the mixture was treated in an ultrasonication bath for 30 min. An aqueous solution of $ZrCl_4$ (0.024 g in 1.25 mL of H_2O) was added dropwise to the GO suspension, and the mixture was stirred for 3 h at room temperature. The mixture was subsequently stirred and heated at 90 °C for 12 h. The solid $ZrO_{2-x}(OH)_{2x}$/GO product was collected by centrifugation, washed with DI-H_2O (3 × 50 mL), and then dispersed into H_2O (10 mL). In the second step, mesoporous silica ($mSiO_2$) layers were grown onto $ZrO_{2-x}(OH)_{2x}$/GO following the procedure described below for the synthesis of $mSiO_2$ platelets. The final product was characterized and displayed a double-layered platelet structure with ultrasmall ZrO_2 nanoparticles in the narrow core.

Synthesis of $mSiO_2$ Platelets. Mesoporous silica platelets ($mSiO_2$) were prepared following a procedure adapted from the literature.[38] GO (30 mg), CTAB (1.00 g, 2.74 mmol), and sodium hydroxide (0.2 g, 5.0 mmol) were first added into deionized water (DI-H_2O, 45 mL), and then the mixture was subjected to ultrasonication for 3 h. The mixture was heated to 40 °C and stirred rapidly for 1 h, and then TEOS (1 mL, 0.94 g, 9.6 mmol) was added in a dropwise fashion to grow mesoporous silica on GO. The reaction mixture was further heated at 40 °C for 24 h. The solid product was collected by centrifugation, washed with DI-H_2O (5 × 50 mL), and washed with ethanol (2 × 50 mL). The solid product was then redispersed into DI-H_2O, and the above $mSiO_2$ growth process was repeated 2 times. Finally, the solid product was dried in an oven at 80 °C and then calcined at 550 °C for 6 h in a box furnace. The final product was then characterized and exhibited a double-layered platelet structure with a narrow empty core.

Synthesis of imp-ZrO_2/mSiO_2. ZrO_2 nanoparticles were deposited throughout the pores and on the external surface of mSiO_2 platelets by the incipient wetness impregnation method. $ZrCl_4$ (0.044 g) as a methanol solution (0.5 mL) was added in a dropwise manner to the previously prepared mSiO_2 platelets (150 mg) while being mixed by a glass rod. The sample was dried in a laboratory oven at 80 °C and then calcined in a box furnace at 550 °C for 6 h. The final product was characterized by STEM (Supplementary Figure S5), which showed a well-dispersed ZrO_2 throughout imp-ZrO_2/mSiO_2 particles.

Preparation of ZrO_2-6/mSiO_2. $ZrO(NO_3)_2 \cdot xH_2O$ (6.374 g) was dissolved in DI-H_2O (15 mL) to form solution A. Urea (10.811 g, 0.18 mol) was dissolved in DI-H_2O (15 mL) to form solution B. Solution A and B were mixed to obtain a solution with the Zr concentration of 0.6 M. The mixture was transferred into a Teflon-lined stainless-steel autoclave and heated at 180 °C for 21 h to give a white crystalline precipitate. The white precipitate was collected, washed with DI-H_2O (2 × 50 mL), and then washed with methanol (2 × 50 mL). The washed sample was redispersed into methanol (38 mL) to obtain suspension C containing ~2.2 g of ZrO_2 nanoparticles. To prepare the ZrO_2-6/mSiO_2 with a ZrO_2 loading of ~5 wt.%, mSiO_2 platelets (50 mg) were mixed with suspension C (35 mg) diluted by methanol (0.25 mL). The mixture was dried in an oven at 60 °C and then calcined at 550 °C for 6 h. The final ZrO_2-6/mSiO_2 product was characterized by STEM (Supplementary Figure S6), which showed that the ZrO_2 nanoparticles are distributed solely on the external surfaces of layered mSiO_2 or are separate aggregates not on the mSiO_2 support.

Synthesis of L-Pt@mSiO_2. The preparation of L-Pt@mSiO_2 followed a modified procedure from the synthesis of L-ZrO_2@mSiO_2. In the first step, urea (0.150 g) was dissolved in DI-H_2O (100 mL), GO (10 mg) was added, and the mixture was treated in an ultrasonication bath for 30 min. Subsequently, an aqueous solution of $H_2PtCl_6 \cdot 6H_2O$ (0.033 g in 1.25 mL) was added dropwise to the GO suspension, and the mixture was stirred for 3 h at room temperature. The mixture was stirred and heated at 90 °C for 12 h. The solid $PtO_{2-x}(OH)_{2x}$/GO product was collected by centrifugation, washed with DI-H_2O (3 × 50 mL), and then dispersed into water (10 mL). In the second step, mesoporous silica (mSiO_2) was grown onto $PtO_{2-x}(OH)_{2x}$/GO following a modified procedure of the one described for the synthesis of L-ZrO_2@mSiO_2, in which $PtO_{2-x}(OH)_{2x}$/GO (rather than $ZrO_{2-x}(OH)_{2x}$/GO) was used as the starting materials for the synthesis. Finally, the L-Pt@mSiO_2 product was obtained after calcination at 550 °C for 6 h and characterized by STEM with the particle size of 3.5 ± 0.8 nm (Supplementary Figure S11c). Like the ZrO_2 nanoparticles of L-ZrO_2@mSiO_2, Pt nanoparticles are localized in the middle of mSiO_2 shells (Supplementary Figure S11a, b).

Characterization of Catalytic Materials

Powder X-ray diffraction (PXRD). The PXRD patterns were collected on a Bruker D8 Advance Twin diffractometer (Ni-filtered Cu Kα radiation with a wavelength of 1.5406 Å, operated at 40 kV and. 40 mA, VANTEC-position-sensitive detector) at a scan speed of 2.0 degrees per min and a step size of 0.02 degrees in 2θ.

Nitrogen gas (N_2) physisorption. The sorption experiments were conducted using a Micromeritics 3Flex surface characterization analyzer at 77 K. The Brunauer-Emmett-Teller (BET) surface area was calculated according to the BET equation, using nitrogen sorption isotherms in the relative pressure range from 0.01 to 0.2. The mesopore size distributions were obtained using BJH method assuming a cylindrical pore model, and the desorption branches of isotherms were used for the calculation.

Inductively coupled plasma mass spectrometry (ICP-MS). The elementary analysis was carried out on a Thermo Scientific X Series II mass spectrometer. The samples (~1.5 mg) are first treated with hydrofluoric acid (80 μL) to etch away silica or dissolve the ZrO_2 particles, and then digested with aqua regia (4 mL). The final solutions were diluted with 2.0 v/v % nitric acid to target concentrations for the ICP-MS measurement. The control samples and blanks were treated following the same procedure described above.

Scanning Transmission Electron Microscopy. High-angle annular dark-field scanning transmission electron microscopy (HAADF-STEM) images and energy dispersive X-ray spectroscopy (EDX) maps were acquired on a FEI Titan Themis 300 probe-corrected scanning transmission electron microscope under 200 kV accelerating voltage. Prior to the imaging, about 1 mg of the ZrO_2-based samples was embedded in 1 mL of Epon epoxy resin and sectioned at 50 nm thickness on a Leica UC6 ultramicrotome with a DiATOME diamond knife.

Solid-State Nuclear Magnetic Resonance Spectroscopy. All solid-state NMR experiments used a Bruker 400 MHz/264 GHz magic angle spinning (MAS) dynamic nuclear polarization (DNP) solid-state (SS)NMR spectrometer equipped with a 3.2 mm low-temperature (100 K) MAS probe, a Bruker AVANCE III console, and a gyrotron microwave source. Samples were impregnated with 16 mM solutions of the TEKPol[73] bisnitroxide polarizing agent[50] in deuterated 1,1,2,2-tetrachloroethane and packed into 3.2 mm sapphire rotors. To reach the positive ^{17}O direct DNP condition,[74] the field of the NMR magnet was decreased by 500 ppm, relative to the field which yields the ^{1}H positive DNP maximum when using nitroxide polarizing agents. Unless otherwise stated, all experiments were conducted at a MAS rate of 12.5 kHz. A 25 kHz effective central transition (CT)-selective radiofrequency (rf) field was used for all ^{17}O pulses and all experiments utilized high-power ^{1}H decoupling. $^{17}O\{^{1}H\}$ phase-shifting effects a smooth transfer of polarization (PRESTO) experiments[46-48] utilized two rotor periods of $R18_1^7$ recoupling.[75] A QCPMG spikelet separation of 625 Hz was used, and 30 echoes were acquired.

All samples were moderately (ca. <20 %) enriched in ^{17}O to enhance sensitivity. Samples were first heated to ca. 430 °C under dynamic vacuum for approximately 8 h to remove surface hydroxyl species. After cooling to room temperature, the samples were treated with minimal amounts of 40% $H_2{}^{17}O$ (Cortecnet) under a nitrogen atmosphere and left to react overnight. Samples were then dried *in vacuo* at room temperature for approximately 8 h.

X-ray Absorption Spectroscopy (XAS). The X-ray absorption spectroscopy measurements at the Zr K-edge (17998 eV) were performed at the Advanced Photon Source (APS) on the bending-magnet beamline 12-BM and 20-BM. A Zr metal foil was used to calibrate the X-ray beam energy and was simultaneously measured with each sample. For each sample, several scans were taken and averaged to gain a better signal-to-noise ratio. The radiation was monochromatized by a Si (111) double-crystal monochromator. The harmonic rejection was accomplished with a Harmonic rejection mirror. The XANES spectroscopy was collected in both transmission and fluorescence mode. And the standards (including the foil) have been measured in transmission mode. XAS data reduction and analysis were processed by Athena software.

Diffuse Reflectance Infrared Fourier Transform Spectroscopy (DRIFTS). Infrared (IR) spectroscopy was carried out on a Nicolet iS50 FTIR instrument with an MCT-B detector, and a Praying Mantis diffuse reflectance accessory and a high temperature reaction chamber from Harrick Scientific. IR spectra were collected with a resolution of 4 cm^{-1}. An average of 64 spectra was used for the reported spectra.

A custom-built gas manifold with carefully calibrated mass flow controllers was employed for delivering purge (Ar, Airgas UHP grade) and reactive (H_2, Airgas UHP grade; D_2 Aldrich 99.8% D) gases. He and H_2 gases were further dried by passing them through Restek indicating purifying columns (model #22020). Both the gas manifold and reaction chamber were gas-tight and were checked for leaks prior to the experiments (leak rates better than 10^{-5} Pa·L/s at all connections).

Briefly, L-ZrO_2@mSiO_2 and ZrO_2-6/mSiO_2 samples were activated by reduction at 550 °C for 3 h in a 3:1 mixture of H_2 in Ar flowing at 40 mL/min. Samples were then cooled to 300 °C in flowing Ar. The spectra were acquired at 300 °C in pure H_2 (or D_2) flowing at 30 mL/min.

Catalysis

Catalytic Hydrogenolysis. The catalytic hydrogenolysis of polyolefins was performed in a glass-lined high-pressure autoclave reactor (250 mL, Parr Instruments) equipped with a mechanical impeller-style stirrer and a thermocouple that extends into the melted polymer.[25] PE (3.0 g, M_n = 20,000, $Đ$ = 4.8) and a catalyst (5.5 mg) were placed into the glass-lined reaction vessel. The reactor was assembled, and the system was evacuated under reduced pressure (100 Pa) and then refilled with Ar (3×). H_2 was introduced to the desired pressure (0.482 MPa) at room temperature, and the reactor was sealed. The reactor was heated to 300 °C, the gauge pressure increased to 0.896 MPa for experiments running 2 – 20 h. All pressure values are reported as the absolute pressure at reaction temperature (0.992 MPa = 0.896 MPa on the pressure gauge). At the end of the designated time, the reactor was allowed to cool to room temperature. The volatile products were sampled by connecting the cooled reactor to a GC sampling loop and analyzed by gas chromatography-flame ionized detector (GC-FID) and GC-thermal conductivity detector (TCD). The mass yield of gas-phase products is obtained from direct GC-calibrated quantitative analysis of C_1-C_9 hydrocarbons separated on an Agilent Technologies 5890 GC system using an Agilent J&W GS-GasPro (0.32 mm × 15 m) capillary column (GC-FID). H_2 was quantified with respect to a He internal standard using a Supelco Carboxen 1000 (15 ft. × 1/8 in. × 2.1 mm SS) packed column (GC-TCD). Dichloromethane was added to the reactor, which was resealed and heated to 100 °C for 8 h. The reactor was cooled, and the mixture was filtered on a Buchner funnel to separate residual insoluble polymer from the dichloromethane-soluble liquid products. The volatile components were evaporated in a rotary evaporator, and the yields of extracted liquid species and solid materials were measured. The soluble materials were analyzed by calibrated gas chromatography-mass spectrometry (GC-MS) using an Agilent Technologies 7890A GC system equipped with an FID or an Agilent Technologies 5975 C inert MSD mass spectrometer on an Agilent J&W DB-5ht ((5%-phenyl)-methylpolysiloxane, 0.25 mm × 30 m × 0.1 μm) capillary column (see Quantification of Liquid Products for details). The solid portion was dissolved in 1,2,4-trichlorobenzene (TCB) at 150 °C and analyzed by high temperature gel permeation chromatography (HT-GPC).

Analysis of Reaction Products. The solid residue was analyzed by HT-GPC (Agilent-Polymer Laboratories 220) to determine the molecular weights (M_n and M_w) and molecular weight distributions ($Đ = M_w/M_n$). The HT-GPC was equipped with refractive index (RI) and viscometry detectors. Monodisperse polyethylene standards (PSS Polymer Standards Service, Inc.) were used for calibration ranging from ~330 Da to ~120 kDa. The column set included 3 Agilent PL-Gel Mixed B columns and 1 PL-Gel Mixed B guard column. TCB containing 0.01 wt% 3,5-di-tert-butyl-4-hydroxytoluene (BHT) was used as the eluent at a flow rate of 1.0 mL/min at 160 °C. The

lubricant samples were prepared in TCB at a concentration of ~5.0 mg/mL and heated at 150 °C for 24 h prior to injection.

Quantification of Liquid Products. The composition of the dichloromethane-extracted liquid products, in terms of amounts of each chain length in the samples, is estimated using our previously reported approach,[25] summarized here briefly for convenience: A GC-MS of the ASTM standard was integrated. A plot of integrated area vs. carbon number allows the determination of response of all C_n (since ASTM standard does not include C_{13}, C_{19}, C_{21}, etc.) by interpolation. The regions of C_6 – C_{20} and C_{20} – C_{40} are linear, but with inequivalent slopes. Therefore, these two regions were fit separately and used as calibration curves for liquid products.[76]

Estimation of C–C Bond Cleavage from Mass Balance. The number average molecular weight M_n can be calculated as the total weight of polymer W divided by the total number of chains N. Under reaction, the number of chains grows over time, with each cleavage reaction producing one new chain. The number of chains may then be expressed as

$$N(t) = N(0) + \int_0^t r_{cut}\,dt \tag{1}$$

where r_{cut} is the rate of cleavage, in cuts per unit time. This may be substituted into the expression for M_n:

$$M_n(t) = \frac{W}{N(t)} = \frac{M_n(0) \cdot W}{W + M_n(0)\int_0^t r_{cut}\,dt} \tag{2}$$

Assuming the cleavage rate is constant and rearranging for r_{cut}:

$$r_{cut} = \frac{W}{t}\left(\frac{1}{M_n(t)} - \frac{1}{M_n(0)}\right) \tag{3}$$

For this relationship to be accurate, the M_n used must be that of the entire population. As the polymer in this work is analyzed in separate groups depending on the molecular weight, these analyses must be combined to determine the overall M_n. As the number average is the first moment of the distribution, the M_n of the entire population is the weighted average of the groups:

$$M_{n,total} = \frac{\sum W_i M_{n,i}}{\sum W_i} \tag{4}$$

where the W_i is the mass of an analyzed group, $M_{n,i}$ is its number averaged molecular weight, and the summations are over all analyzed groups. This result is valid for any number of groups and is true even when polymers of the same size may exist in multiple groups. $M_{n,total}$ may be then used to estimate the C–C bond cleavage rate per eq 3.

Computational Catalysis Study

Density Functional Theory Calculations. DFT calculations related to the reaction network of hexane activation over the ZrO_xH_y models supported on the (-111) surface of monoclinic ZrO_2 were performed using the periodic plane wave code Vienna ab initio simulation package (VASP 5.4).[77-80] The ion-electron interaction was described by pseudopotentials constructed within the projector augmented wave (PAW) framework.[81,82] The Perdew-Burke-Ernzerhof (PBE)[83] functional form of the generalized gradient approximation (GGA) was used to treat electron exchange–correlation effects, and Grimme's DFT-D3[84] method was used to semiempirically describe the van der Waals interactions. To partially account for the self-interaction errors

associated with the GGA-PBE functional, we used the DFT + U methodology by setting the U - J value for the 4d states of Zr to 4 eV.[34,85] For the structure relaxation, we sampled the Brillouin zone by a 2 x 2 x 1 Monkhorst-Pack (MP)[86] k-mesh applying a Gaussian smearing approach (σ = 0.05 eV) with a plane-wave kinetic energy cutoff of 500 eV. All the calculations included dipole and quadrupole corrections for the energies as implemented in VASP using a modified version of the Makov and Payne method,[87] and Harris–Foulke-type corrections[88] were applied for the forces. The transition state structures were determined by the climbing image nudged elastic band (CI-NEB)[89-91] and Dimer methods.[92,93]

Microkinetic Modeling of Hexane Hydrogenolysis over the ZrO_xH_y/m-ZrO_2 Model. A mean-field microkinetic model was developed to elucidate the reaction mechanism of hexane hydrogenolysis over the ZrO_xH_y/m-ZrO_2 model. The rate (r_i) of an elementary reaction defined by the sum of forward ($r_{for,i}$) and reverse ($r_{rev,i}$) reaction rates is presented in eq 5.

$$r_i = r_{for,i} - r_{rev,i} = k_{for,i} \prod_{j=1}^{N} \left(X_j^{-\nu_{ji}}\right)_{\nu_{ji}<0} - k_{rev,i} \prod_{j=1}^{M} \left(X_j^{\nu_{ji}}\right)_{\nu_{ji}>0} \tag{5}$$

ν_{ji} is the stoichiometric coefficient of species j, and X_j is either the fractional coverage of surface species j (θ_j) or partial pressure of gas species j (P_j). The forward ($k_{for,i}$) or reverse ($k_{rev,i}$) rate constants of the reaction step, i, are defined as:

$$k_i = \frac{k_B T}{h} e^{-\frac{G_{a,i}}{k_B T}} \tag{6}$$

$$G_{a,i} = E_{a,i} - k_B T \cdot ln\left(\frac{q_{TS,vib,i}}{q_{IS,vib,i}}\right) \tag{7}$$

where k_B is the Boltzmann constant, T is the temperature (K), and h is the Planck constant. To calculate the free energy of activation (G_a) according to classical harmonic transition state theory,[94] the zero-point corrected energy (E_a) and entropy terms calculated from the vibrational partition functions of the transition state ($q_{TS,vib}$) and initial state ($q_{IS,vib}$) were obtained from DFT calculations. We shifted all frequencies below 50 cm^{-1} to 50 cm^{-1} for surface species to reduce the errors in the harmonic approximation for small vibrational frequencies (these frequencies in effect cancel out).[95]

Collision theory was used to calculate the rate constant of adsorption of any gas phase species as,

$$k_{ads,i} = \frac{1}{N_0 \sqrt{2\pi m_{g,i} k_B T}} \tag{8}$$

where N_0 is the number of active sites per unit surface area (2.5×10^{19} sites/m^2) and m_g is the molecular weight of the gas molecule. The rate constant of desorption was calculated using the rate constant of adsorption and the equilibrium constant (K_i) as $k_{des,i} = k_{ads,i}/K_i$. K_i of an elementary reaction step was calculated using the expression:

$$K_i = e^{\frac{-\Delta G_i}{k_B T}} \tag{9}$$

where ΔG_i is the free energy of the adsorption process. Here, the entropy term for hexane adsorption was calculated using the empirical formula, $S_{ad}^0(T) = 0.70 \times S_{gas}^0(T) - 3.3R$, derived by Campbell and Sellers.[96]

A set of coupled ordinary differential equations (ODEs) for the elementary reactions was numerically solved until steady state is reached using the Matlab ODE15s solver.[97,98] Each elementary ODE is formulated as,

$$\frac{d\theta_j}{dt} = \sum_i \nu_{j,i} r_{for,i} - \sum_i \nu_{j,i} r_{rev,i} \tag{10}$$

using an overall site balance equation described as,

$$\sum_j \theta_j = 1 \tag{11}$$

Continuous Stirred-Tank Reactor (CSTR) Model. Assuming an isothermal and isobaric CSTR model, the species balance for the ideal gas phase reactants and products can be written as,

$$\frac{\partial y_{i,gas}}{\partial\left(\frac{t}{\tau}\right)} = y_{i,gas,0} - y_{i,gas}\left(1 + \tau \times \alpha \sum_i r_{i,gas}\right) + \tau \times \alpha \times r_{i,gas} \tag{12}$$

where $y_{i,gas}$ is the mole fraction of gas species i, t is the time, $y_{i,gas,0}$ is the inlet mole fraction of gas species i, τ is a residence time defined as the ratio of the total mole number of gas molecules in the reactor over the total feed flow rate at reactor entrance conditions $\tau = N_{tot,0}/F_{tot,0}$, α is the total number of active sites in the reactor over the total mole number of gas molecules in the reactor $N_{cat}/N_{tot,0}$, and $r_{i,gas}$ is a generation rate of gas species i per active site. Due to a lack of experimental information to calculate the parameters α and τ, we fixed $\alpha = 1\times10^{-3}$ assuming that the surface density of catalyst is constant throughout the examination of the catalytic performance under various conditions and examined $y_{i,gas}$ at various residence times at fixed temperature.[99] Ultimately, only the product of $\alpha \times \tau = N_{cat}/F_{tot,0}$ determines the steady state reactor outlet composition, $y_{i,gas}$, and the overall conversion (which could be used to get meaningful values of the product of α and τ).

Parahydrogen Induced Polarization Study

Conditions. Hydrogenation of propene over L-ZrO_2@mSiO_2 was examined by Adiabatic Longitudinal Transport After Dissociation Engenders Net Alignment (ALTADENA)[70] NMR experiments using 99% para-enriched H_2 (pH_2). The pH_2 gas was produced by flowing H_2 (Airgas, UHP) through a cryocooled pH_2 converter (Advanced Research Systems, Inc.) with a catalyst compartment packed with 46 g of FeO(OH) (Sigma-Aldrich) at 20 K. The pH_2 and propene (Airgas, UHP) were mixed by combining the outlets of the mass flow controllers (MFC, Alicat) for each gas with a total flow rate of 60 sccm and a pH_2/propene ratio of 5/1. Experiments were performed using 64.9 mg of L-ZrO_2@mSiO_2 packed into a 304 stainless-steel (SS) reactor tube (McMaster-Carr, 5 cm length, 0.25-inch O.D., 0.152-inch I.D.). The catalyst material was held in place using quartz wool and porous 316L SS frits (McMaster-Carr, 10 μm pore size) on both ends of the reactor tube. The reactor was mounted in the 4.5 mT fringe field of the 9.4 T Bruker Avance wide bore magnet. The catalyst was pretreated by flowing an H_2/N_2 mixture (total flow rate of 50 mL/min, 10% H_2) through the reactor at 550 °C for 6 h. Propene hydrogenation was carried out by

flowing the pH_2/propene mixture through the catalyst bed at 300 °C at an inlet pressure of 0.294 MPa. The reactor effluent was then transported to the detection coil of a Varian 400 MHz Triple-Resonance IFC flow NMR probe at high field (9.4 T) via flow of the gas through approximately 110 cm of 1/16-inch O.D. PEEK tubing (0.020-inch I.D.). The ^{1}H NMR spectrum of the reactor effluent was collected on a 400 MHz Varian VNMRS spectrometer. The continous flow (CF) hyperpolarized spectrum was acquired by signal averaging of 32-transients using a recycle delay (d1) of 1 s and an acquisition time (AT) of 0.2 s. The thermally polarized spectrum was acquired after sealing the gas in the NMR probe and signal averaging of 32-transients using a d1 of 5 s and an AT of 0.5 s. The propene hydrogenation with nH_2 (25% para-enrichment) was also performed under identical conditions. The pure ALTADENA spectrum was obtained by subtracting the CF NMR spectrum acquired using nH_2 from the spectrum acquired with 99% pH_2. To ensure that the ALTADENA signal is due to hydrogenation over the L-ZrO_2@mSiO_2 catalyst and not from any other contaminant or metal in the reactor system, control experiments were performed using 99% pH_2 and a reactor tube packed only with an inert filler material (quartz wool). The experimental conditions were otherwise identical. The empty reactor did not yield any detectable conversion, but it did produce a small propane ALTADENA signal with intensity of about 5% relative to the signal acquired using the L-ZrO_2@mSiO_2 catalyst at 300 °C. The small background NMR signal appears to arise from the SS surfaces in the reactor and has been observed in our lab previously.

Calculation of Conversion. The fractional conversion of propene to propane (PA) was calculated from the thermally polarized (TP) spectrum using the following equations:

$$S^{TP}_{PA,1H} = \frac{S^{TP}_{PA,CH_3}/6 - X_{imp} \cdot S^{TP}_{propene,CH}}{1 + X_{imp}} \tag{13}$$

$$\chi = \left(\frac{S^{TP}_{PA,1H}}{S^{TP}_{PA,1H} + S^{TP}_{propene,CH}} \right) \times 100\% \tag{14}$$

where

χ = Conversion of propene to propane (PA).

S^{TP}_{PA,CH_3} = Measured integral of the PA CH_3 peak in thermally polarized spectrum.

$S^{TP}_{propene,CH}$ = Measured integral of the propene CH peak in thermally polarized spectrum.

$S^{TP}_{PA,CH}$ = Calculated integral per proton of PA after the correction of PA impurity.

X_{imp} = Percent impurity of PA in stock propene, 0.26%.

Calculation of Signal Enhancement. The experimental ALTADENA NMR signal enhancement (ε) was evaluated by subtracting the ALTADENA integral of the PA CH_3 for the experiment using SS cartridge with inert fillers from that using L-ZrO_2@mSiO_2, then comparing it to the PA CH_3 peak integral of the thermally polarized spectrum:

$$\varepsilon = \frac{S^{ZrO_2}_{PA,CH_3} - S^{SS}_{PA,CH_3}}{S^{TP}_{PA,1H}} \tag{15}$$

where

$S_{PA,CH_3}^{ZrO_2}$ = integral of the PA CH_3 peak in the ALTADENA spectrum of experiments catalyzed by L-ZrO_2@mSiO_2

S_{PA,CH_3}^{SS} = integral of the PA CH_3 peak in the ALTADENA spectrum of experiments catalyzed by SS cartridge with inert fillers

Calculation of Pairwise Selectivity. The pairwise selectivity (φ) was obtained by dividing the experimental ALTADENA NMR signal enhancement (ε) by the theoretical value (ε^{theor}, assuming 100% pairwise addition), as in eq 16.

$$\varphi = \frac{\varepsilon}{\varepsilon^{theor}} \times 100\% \tag{16}$$

For the CH_3 proton of PA, the theoretical ALTADENA signal enhancement was obtained from eq 17.[100,101]

$$\varepsilon_{ALTADENA}^{theor} = \frac{2k_B T\left(4\chi_p - 1\right)}{3\hbar\gamma_H B_0} \tag{17}$$

where T is the temperature, γ_H is the ^{1}H gyromagnetic ratio (in rad/s), B_0 is the static magnetic field, and χ_p is the para-enrichment. When T = 300 K, B_0 = 9.4 T, and χ_p = 99%, $\varepsilon_{ALTADENA}^{theor}$ =31524.

Due to the back-conversion of pH_2 to oH_2 by the catalyst during the propene hydrogenation, the actual para-enrichment of the H_2 gas within the reactor could be lower than 99%. Indeed, the para-enrichment observed under reaction conditions was only χ'_p = 58.7%, estimated from eq 18

$$\chi'_p = \left(1 - \frac{3S_{pH_2}}{4S_{nH_2}}\right) \times 100\% \tag{18}$$

where S_{pH_2} and S_{nH_2} represent the integrals of the oH_2 peak in spectra acquired with pH_2 and nH_2, respectively, in the presence of propene, under reaction conditions. The corrected pairwise selectivity (φ') was then obtained using eq 16 through eq 18.

Conversion	Signal enhancement	Pairwise selectivity (assuming 99% pH_2)	Corrected pairwise selectivity	Observed pH_2 enrichment
5.42% ± 0.55%	78.5 ± 11.4	0.255% ± 0.036%	0.558% ± 0.079%	58.7%

Acknowledgements

This work was supported by the Institute for Cooperative Upcycling of Plastics (iCOUP), an Energy Frontier Research Center funded by the U.S. Department of Energy (DOE), Office of Basic Energy Sciences. Ames Laboratory is operated by Iowa State University under Contract DE-AC-02-07CH11358, and Argonne National Laboratory is operated by University of Chicago Argonne LLC under Contract DE-AC-02-06CH11357 (Argonne National Laboratory). SCA and AH acknowledge partial support from the South Carolina Smart State Center for Strategic Approaches to the Generation of Electricity (SAGE). Parahydrogen labeling experiments were supported by National Science Foundation grant CHE-2108306. This research used resources of the Advanced Photon Source, a U.S. Department of Energy (DOE) Office of Science User Facility operated for the DOE Office of Science by Argonne National Laboratory under Contract No. DE-AC02-06CH11357. Computational resources are provided by XSEDE resources located at San Diego

Supercomputer Center and Texas Advanced Computing Center (Grant No. TG-CTS090100) as well as the National Energy Research Scientific Computing Center (NERSC) under Contract No. DE-AC02-05CH11231.

Author Contributions

S.C. prepared and characterized zirconia catalysts under the direction of W.H. Catalytic experiments were performed by A.T. and M.S., and analysis of liquid products was performed by A.T., M.S., Y.-Y.W., X.W. and L.Q. guided by A.D.S. and W.H. GPC was performed by R.A.H. under supervision of M.D. Theoretical calculations were performed by K.-E.Y. and S.C.A., directed by A.H., and numbers of C-C bond cleavage steps were calculated by R.Y. using the model created by B.P. Characterization by SSNMR was conducted by A.L.P. under the direction of F.A.P.; XAS by L.F., T.L. and B.L., ICP-MS by S.C. and X.W., DRIFT experiments by S.A. and K.P, and PHIP experiments by T.Y.Z., M.P.L, and C.R.B. The manuscript was composed by S.C., A.T., K.-E.Y., A.H., W.H., and A.D.S. with contributions from all other co-authors.

Competing Interests

The authors declare no competing interests.

Additional Information

Supplementary Information includes additional synthesis and characterization data for the materials used in the main text and catalytic reaction outcomes. Details are also given regarding some control SSNMR and DFT experiments that were used to verify the assignments of the spectra.

Data Availability Statement

The authors declare that the data supporting the findings of this study are available within the paper and its supplementary information files.

References

1 Amakawa, K., Wrabetz, S., Kröhnert, J., Tzolova-Müller, G., Schlögl, R. & Trunschke, A. In Situ Generation of Active Sites in Olefin Metathesis. *J. Am. Chem. Soc.* **134**, 11462-11473 (2012).

2 Lwin, S. & Wachs, I. E. Olefin Metathesis by Supported Metal Oxide Catalysts. *ACS Catal.* **4**, 2505-2520 (2014).

3 Wang, A., Li, J. & Zhang, T. Heterogeneous Single-Atom Catalysis. *Nat. Rev. Chem.* **2**, 65-81 (2018).

4 Sinfelt, J. H., Taylor, W. F. & Yates, D. J. C. Catalysis over Supported Metals. III. Comparison of Metals of Known Surface Area for Ethane Hydrogenolysis. *J. Phys. Chem.* **69**, 95-101 (1965).

5 Blakely, D. W. & Somorjai, G. A. The Dehydrogenation and Hydrogenolysis of Cyclohexane and Cyclohexene on Stepped (High Miller Index) Platinum Surfaces. *J. Catal.* **42**, 181-196 (1976).

6 Gillespie, W. D., Herz, R. K., Petersen, E. E. & Somorjai, G. A. The Structure Sensitivity of n-Heptane Dehydrocyclization and Hydrogenolysis Catalyzed by Platinum Single Crystals at Atmospheric Pressure. *J. Catal.* **70**, 147-159 (1981).

7 Locatelli, F., Candy, J.-P., Didillon, B., Niccolai, G. P., Uzio, D. & Basset, J.-M. Hydrogenolysis of Cyclohexane over Ir/SiO_2 Catalyst: A Mechanistic Study of Carbon−Carbon Bond Cleavage on Metallic Surfaces. *J. Am. Chem. Soc.* **123**, 1658-1663 (2001).

8 Flaherty, D. W. & Iglesia, E. Transition-State Enthalpy and Entropy Effects on Reactivity and Selectivity in Hydrogenolysis of n-Alkanes. *J. Am. Chem. Soc.* **135**, 18586-18599 (2013).

9 Zhang, S., Liu, D., Deng, W. & Que, G. A Review of Slurry-Phase Hydrocracking Heavy Oil Technology. *Energy Fuels* **21**, 3057-3062 (2007).

10 Weitkamp, J. Catalytic Hydrocracking—Mechanisms and Versatility of the Process. *ChemCatChem* **4**, 292-306 (2012).

11 Geyer, R., Jambeck, J. R. & Law, K. L. Production, Use, and Fate of All Plastics Ever Made. *Sci. Adv.* **3**, e1700782 (2017).

12 De Smet, M. The New Plastics Economy: Rethinking the Future of Plastics. Report No. 080116, (Ellen Macarthur Foundation, 2016).

13 Lau, W. W. Y., Shiran, Y., Bailey, R. M., Cook, E., Stuchtey, M. R., Koskella, J. *et al.* Evaluating Scenarios Toward Zero Plastic Pollution. *Science* **369**, 1455 (2020).

14 Borrelle, S. B., Ringma, J., Law, K. L., Monnahan, C. C., Lebreton, L., McGivern, A. *et al.* Predicted Growth in Plastic Waste Exceeds Efforts to Mitigate Plastic Pollution. *Science* **369**, 1515 (2020).

15 Celik, G., Kennedy, R. M., Hackler, R. A., Ferrandon, M., Tennakoon, A., Patnaik, S. *et al.* Upcycling Single-Use Polyethylene into High-Quality Liquid Products. *ACS Cent. Sci.* **5**, 1795-1803 (2019).

16 Hackler, R. A., Vyavhare, K., Kennedy, R. M., Celik, G., Kanbur, U., Griffin, P. J. *et al.* Synthetic Lubricants Derived from Plastic Waste and their Tribological Performance. *ChemSusChem* **14**, 4181-4189 (2021).

17 Liu, S., Kots, P. A., Vance, B. C., Danielson, A. & Vlachos, D. G. Plastic Waste to Fuels by Hydrocracking at Mild Conditions. *Sci. Adv.* **7**, eabf8283 (2021).

18 Kots, P. A., Liu, S., Vance, B. C., Wang, C., Sheehan, J. D. & Vlachos, D. G. Polypropylene Plastic Waste Conversion to Lubricants over Ru/TiO_2 Catalysts. *ACS Catal.* **11**, 8104-8115 (2021).

19 Rorrer, J. E., Beckham, G. T. & Román-Leshkov, Y. Conversion of Polyolefin Waste to Liquid Alkanes with Ru-Based Catalysts under Mild Conditions. *JACS Au* **1**, 8-12 (2021).

20 Nakaji, Y., Tamura, M., Miyaoka, S., Kumagai, S., Tanji, M., Nakagawa, Y. *et al.* Low-temperature Catalytic Upgrading of Waste Polyolefinic Plastics into Liquid Fuels and Waxes. *Appl. Catal. B* **285**, 119805 (2021).

21 Jaydev, S. D., Martín, A. J. & Pérez-Ramírez, J. Direct Conversion of Polypropylene into Liquid Hydrocarbons on Carbon-Supported Platinum Catalysts. *ChemSusChem* **14**, 5179-5185 (2021).

22 O'Reilly, M. E., Dutta, S. & Veige, A. S. β-Alkyl Elimination: Fundamental Principles and Some Applications. *Chem. Rev.* **116**, 8105-8145 (2016).

23 Dufaud, V. & Basset, J.-M. Catalytic Hydrogenolysis at Low Temperature and Pressure of Polyethylene and Polypropylene to Diesels or Lower Alkanes by a Zirconium Hydride Supported on Silica-Alumina: A Step Toward Polyolefin Degradation by the Microscopic Reverse of Ziegler–Natta Polymerization. *Angew. Chem. Int. Ed.* **37**, 806-810 (1998).

24 Kanbur, U., Zang, G., Paterson, A. L., Chatterjee, P., Hackler, R. A., Delferro, M. *et al.* Catalytic Carbon-Carbon Bond Cleavage and Carbon-Element Bond Formation Give New Life for Polyolefins as Biodegradable Surfactants. *Chem* **7**, 1347-1362 (2021).
25 Tennakoon, A., Wu, X., Paterson, A. L., Patnaik, S., Pei, Y., LaPointe, A. M. *et al.* Catalytic Upcycling of High-density Polyethylene Via a Processive Mechanism. *Nat. Catal.* **3**, 893-901 (2020).
26 Wu, X., Tennakoon, A., Yappert, R., Esveld, M., Ferrandon, M. S., Hackler, R. A. *et al.* Size-Controlled Nanoparticles Embedded in a Mesoporous Architecture Leading to Efficient and Selective Hydrogenolysis of Polyolefins. *J. Am. Chem. Soc.* **144**, 5323-5334 (2022).
27 Xiao, C., Maligal-Ganesh, R. V., Li, T., Qi, Z., Guo, Z., Brashler, K. T. *et al.* High-Temperature-Stable and Regenerable Catalysts: Platinum Nanoparticles in Aligned Mesoporous Silica Wells. *ChemSusChem* **6**, 1915-1922 (2013).
28 Lyu, X., Wu, X., Liu, Y., Huang, W., Lee, B. & Li, T. Synthesis and Characterization of Mesoporous Silica Nanoparticles Loaded with Pt Catalysts. *Catalysts* **12** (2022).
29 Kobayashi, T., Singappuli-Arachchige, D., Wang, Z., Slowing, I. I. & Pruski, M. Spatial Distribution of Organic Functional Groups Supported on Mesoporous Silica Nanoparticles: A Study by Conventional and DNP-Enhanced ^{29}Si Solid-state NMR. *Phys. Chem. Chem. Phys.* **19**, 1781-1789 (2017).
30 Kobayashi, T. & Pruski, M. Spatial Distribution of Silica-Bound Catalytic Organic Functional Groups Can Now Be Revealed by Conventional and DNP-Enhanced Solid-State NMR Methods. *ACS Catal.* **9**, 7238-7249 (2019).
31 Kondo, J., Domen, K., Maruya, K.-i. & Onishi, T. Infrared Studies of Ethene Hydrogenation Over ZrO_2. Part 3.—Reaction Mechanism. *J. Chem. Soc., Faraday Trans.* **88**, 2095-2099 (1992).
32 Hoang, D. L. & Lieske, H. Effect of Hydrogen Treatments on ZrO_2 and Pt/ZrO_2 Catalysts. *Catal. Lett.* **27**, 33-42 (1994).
33 Utami, M., Trisunaryanti, W., Shida, K., Tsushida, M., Kawakita, H., Ohto, K. *et al.* Hydrothermal Preparation of a Platinum-Loaded Sulphated Nanozirconia Catalyst for the Effective Conversion of Waste Low Density Polyethylene into Gasoline-Range Hydrocarbons. *RSC Adv.* **9**, 41392-41401 (2019).
34 Puigdollers, A. R., Tosoni, S. & Pacchioni, G. Turning a Nonreducible into a Reducible Oxide via Nanostructuring: Opposite Behavior of Bulk ZrO_2 and ZrO_2 Nanoparticles Toward H_2 Adsorption. *J. Phys. Chem. C* **120**, 15329-15337 (2016).
35 Zhang, Y., Zhao, Y., Otroshchenko, T., Lund, H., Pohl, M.-M., Rodemerck, U. *et al.* Control of Coordinatively Unsaturated Zr Sites in ZrO_2 for Efficient C–H Bond Activation. *Nat. Commun.* **9**, 3794 (2018).
36 Arce-Ramos, J.-M., Grabow, L. C., Handy, B. E. & Cárdenas-Galindo, M.-G. Nature of Acid Sites in Silica-Supported Zirconium Oxide: A Combined Experimental and Periodic DFT Study. *J. Phys. Chem. C* **119**, 15150-15159 (2015).
37 Yang, S., Feng, X., Wang, L., Tang, K., Maier, J. & Müllen, K. Graphene-Based Nanosheets with a Sandwich Structure. *Angew. Chem. Int. Ed.* **49**, 4795-4799 (2010).
38 Wang, Z.-M., Wang, W., Coombs, N., Soheilnia, N. & Ozin, G. A. Graphene Oxide−Periodic Mesoporous Silica Sandwich Nanocomposites with Vertically Oriented Channels. *ACS Nano* **4**, 7437-7450 (2010).

39 Wang, Z.-M., Peng, W., Takenaka, Y., Yoshizawa, N., Kosuge, K., Wang, W. *et al.* Sandwich-Type Nanocomposite of Reduced Graphene Oxide and Periodic Mesoporous Silica with Vertically Aligned Mesochannels of Tunable Pore Depth and Size. *Adv. Func. Mater.* **27**, 1704066 (2017).

40 Williams, D. B. & Carter, C. B. in *Transmission Electron Microscopy: A Textbook for Materials Science* (eds David B. Williams & C. Barry Carter) 283-309 (Springer US, 2009).

41 Sharma, A., Varshney, M., Chae, K. H., Shin, H. J. & Won, S. O. Investigation on the Local Electronic/Atomic Structure Properties Using XANES/EXAFS and Photocatalyst Application of $Zr_{1-x}Cu_xO_2$ ($0 \leqslant x \leqslant 0.2$). *Curr. Appl Phys.* **16**, 1326-1333 (2016).

42 Wang, X., Chen, Z., Zhao, X., Yao, T., Chen, W., You, R. *et al.* Regulation of Coordination Number over Single Co Sites: Triggering the Efficient Electroreduction of CO_2. *Angew. Chem. Int. Ed.* **57**, 1944-1948 (2018).

43 Lesage, A., Auger, C., Caldarelli, S. & Emsley, L. Determination of Through-Bond Carbon−Carbon Connectivities in Solid-State NMR Using the INADEQUATE Experiment. *J. Am. Chem. Soc.* **119**, 7867-7868 (1997).

44 Rossini, A. J., Zagdoun, A., Lelli, M., Lesage, A., Copéret, C. & Emsley, L. Dynamic Nuclear Polarization Surface Enhanced NMR Spectroscopy. *Acc. Chem. Res.* **46**, 1942-1951 (2013).

45 Shen, L., Wu, X.-P., Wang, Y., Wang, M., Chen, J., Li, Y. *et al.* ^{17}O Solid-State NMR Studies of ZrO_2 Nanoparticles. *J. Phys. Chem. C* **123**, 4158-4167 (2019).

46 Zhao, X., Hoffbauer, W., Schmedt auf der Günne, J. & Levitt, M. H. Heteronuclear Polarization Transfer by Symmetry-Based Recoupling Sequences in Solid-State NMR. *Solid State Nucl. Magn. Reson.* **26**, 57-64 (2004).

47 van Beek, J. D., Dupree, R. & Levitt, M. H. Symmetry-Based Recoupling of ^{17}O–^{1}H Spin Pairs in Magic-Angle Spinning NMR. *J. Magn. Reson.* **179**, 38-48 (2006).

48 Perras, F. A., Kobayashi, T. & Pruski, M. Natural Abundance ^{17}O DNP Two-Dimensional and Surface-Enhanced NMR Spectroscopy. *J. Am. Chem. Soc.* **137**, 8336-8339 (2015).

49 Maleki, F. & Pacchioni, G. DFT Study of ^{17}O NMR Spectroscopy Applied to Zirconia Surfaces and Nanoparticles. *J. Phys. Chem. C* **123**, 21629-21638 (2019).

50 Perras, F. A., Boteju, K. C., Slowing, I. I., Sadow, A. D. & Pruski, M. Direct ^{17}O Dynamic Nuclear Polarization of Single-Site Heterogeneous Catalysts. *Chem. Commun.* **54**, 3472-3475 (2018).

51 Lamparter, P. & Kniep, R. Structure of Amorphous Al_2O_3. *Physica B* **234-236**, 405-406 (1997).

52 Petkov, V., Holzhüter, G., Tröge, U., Gerber, T. & Himmel, B. Atomic-Scale Structure of Amorphous TiO_2 by Electron, X-ray Diffraction and Reverse Monte Carlo Simulations. *J. Non-Cryst. Solids* **231**, 17-30 (1998).

53 Lee, S. K., Lee, S. B., Park, S. Y., Yi, Y. S. & Ahn, C. W. Structure of Amorphous Aluminum Oxide. *Phys. Rev. Lett.* **103**, 095501 (2009).

54 Buchholz, D. B., Ma, Q., Alducin, D., Ponce, A., Jose-Yacaman, M., Khanal, R. *et al.* The Structure and Properties of Amorphous Indium Oxide. *Chem. Mater.* **26**, 5401-5411 (2014).

55 Strand, J., Kaviani, M., Gao, D., El-Sayed, A.-M., Afanas'ev, V. V. & Shluger, A. L. Intrinsic Charge Trapping in Amorphous Oxide Films: Status and Challenges. *J. Phys.: Condens. Matter* **30**, 233001 (2018).

56 Onishi, T., Abe, H., Maruya, K.-i. & Domen, K. IR Spectra of Hydrogen Adsorbed on ZrO_2. *J. Chem. Soc., Chem. Commun.*, 617-618 (1985).

57 Kondo, J., Sakata, Y., Domen, K., Maruya, K.-i. & Onishi, T. Infrared Study of Hydrogen Adsorbed on ZrO_2. *J. Chem. Soc., Faraday Trans.* **86**, 397-401 (1990).

58 Trunschke, A., Hoang, D. L. & Lieske, H. In Situ FTIR Studies of High-Temperature Adsorption of Hydrogen on Zirconia. *J. Chem. Soc., Faraday Trans.* **91**, 4441-4444 (1995).

59 Puigdollers, A. R., Illas, F. & Pacchioni, G. Reduction of Hydrogenated ZrO_2 Nanoparticles by Water Desorption. *ACS Omega* **2**, 3878-3885 (2017).

60 Hicks, K. E., Rosen, A. S., Syed, Z. H., Snurr, R. Q., Farha, O. K. & Notestein, J. M. Zr_6O_8 Node-Catalyzed Butene Hydrogenation and Isomerization in the Metal–Organic Framework NU-1000. *ACS Catal.* **10**, 14959-14970 (2020).

61 Walsh, P. J., Hollander, F. J. & Bergman, R. G. Generation, Alkyne Cycloaddition, Arene Carbon-Hydrogen Activation, Nitrogen-Hydrogen Activation and Dative Ligand Trapping Reactions of the First Monomeric Imidozirconocene (Cp_2Zr:NR) Complexes. *J. Am. Chem. Soc.* **110**, 8729-8731 (1988).

62 Cummins, C. C., Baxter, S. M. & Wolczanski, P. T. Methane and Benzene Activation Via Transient (*tert*-$Bu_3SiNH)_2Zr$=NSi-*tert*-Bu_3. *J. Am. Chem. Soc.* **110**, 8731-8733 (1988).

63 Cundari, T. R., Klinckman, T. R. & Wolczanski, P. T. Carbon−Hydrogen Bond Activation by Titanium Imido Complexes. Computational Evidence for the Role of Alkane Adducts in Selective C−H Activation. *J. Am. Chem. Soc.* **124**, 1481-1487 (2002).

64 Hoyt, H. M., Michael, F. E. & Bergman, R. G. C-H Bond Activation of Hydrocarbons by an Imidozirconocene Complex. *J. Am. Chem. Soc.* **126**, 1018-1019 (2004).

65 Gell, K. I. & Schwartz, J. Hydrogenation of d^0 complexes: zirconium(IV) alkyl hydrides. *J. Am. Chem. Soc.* **100**, 3246-3248 (1978).

66 Schwartz, J. & Ward, M. D. Silica-Supported Zirconium Hydrides as Isomerization or Hydrogenation Catalysts for Long-Chain Olefins. *J. Mol. Catal.* **8**, 465-469 (1980).

67 Yermakovt, Y. I., Ryndin, Y. A., Alekseev, O. S., Kochubey, D. I., Shmachkov, V. A. & Gergert, N. I. Hydride Complexes of Titanium and Zirconium Attached to SiO_2 as Hydrogenation Catalysts. *J. Mol. Catal.* **49**, 121-132 (1989).

68 Corker, J., Lefebvre, F., Lécuyer, C., Dufaud, V., Quignard, F., Choplin, A. *et al.* Catalytic Cleavage of the C-H and C-C Bonds of Alkanes by Surface Organometallic Chemistry: An EXAFS and IR Characterization of a Zr-H Catalyst. *Science* **271**, 966-969 (1996).

69 Lecuyer, C., Quignard, F., Choplin, A., Olivier, D. & Basset, J.-M. Surface Organometallic Chemistry on Oxides: Selective Catalytic Low-Temperature Hydrogenolysis of Alkanes by a Highly Electrophilic Zirconium Hydride Complex Supported on Silica. *Angew. Chem. Int. Ed. Engl.* **30**, 1660-1661 (1991).

70 Pravica, M. G. & Weitekamp, D. P. Net NMR Alignment by Adiabatic Transport of Parahydrogen Addition Products to High Magnetic Field. *Chem. Phys. Lett.* **145**, 255-258 (1988).

71 Bowers, C. R. & Weitekamp, D. P. Parahydrogen and Synthesis Allow Dramatically Enhanced Nuclear Alignment. *J. Am. Chem. Soc.* **109**, 5541-5542 (1987).
72 Zhao, E. W., Zheng, H., Zhou, R., Hagelin-Weaver, H. E. & Bowers, C. R. Shaped Ceria Nanocrystals Catalyze Efficient and Selective Para-Hydrogen-Enhanced Polarization. *Angew. Chem. Int. Ed.* **54**, 14270-14275 (2015).
73 Zagdoun, A., Casano, G., Ouari, O., Schwarzwälder, M., Rossini, A. J., Aussenac, F. *et al.* Large Molecular Weight Nitroxide Biradicals Providing Efficient Dynamic Nuclear Polarization at Temperatures up to 200 K. *J. Am. Chem. Soc.* **135**, 12790-12797 (2013).
74 Michaelis, V. K., Corzilius, B., Smith, A. A. & Griffin, R. G. Dynamic Nuclear Polarization of ^{17}O: Direct Polarization. *J. Phys. Chem. B* **117**, 14894-14906 (2013).
75 Carravetta, M., Edén, M., Zhao, X., Brinkmann, A. & Levitt, M. H. Symmetry Principles for the Design of Radiofrequency Pulse Sequences in the Nuclear Magnetic Resonance of Rotating Solids. *Chem. Phys. Lett.* **321**, 205-215 (2000).
76 Göröcs, N., Mudri, D., Mátyási, J. & Balla, J. The Determination of GC–MS Relative Molar Responses of Some n-Alkanes and their Halogenated Analogs. *J. Chromatogr. Sci.* **51**, 138-145 (2012).
77 Kresse, G. & Hafner, J. Ab Initio Molecular-Dynamics Simulation of the Liquid-Metal--Amorphous-Semiconductor Transition in Germanium. *Phys. Rev. B* **49**, 14251-14269 (1994).
78 Kresse, G. Ab Initio Molecular Dynamics for Liquid Metals. *J. Non-Cryst. Solids* **192-193**, 222-229 (1995).
79 Kresse, G. & Furthmüller, J. Efficiency of Ab-Initio Total Energy Calculations for Metals and Semiconductors Using a Plane-Wave Basis Set. *Comput. Mater. Sci* **6**, 15-50 (1996).
80 Kresse, G. & Furthmüller, J. Efficient Iterative Schemes for Ab Initio Total-Energy Calculations Using a Plane-Wave Basis Set. *Phys. Rev. B* **54**, 11169-11186 (1996).
81 Blöchl, P. E. Projector Augmented-Wave Method. *Phys. Rev. B* **50**, 17953-17979 (1994).
82 Kresse, G. & Joubert, D. From Ultrasoft Pseudopotentials to the Projector Augmented-Wave Method. *Phys. Rev. B* **59**, 1758-1775 (1999).
83 Perdew, J. P., Burke, K. & Ernzerhof, M. Generalized Gradient Approximation Made Simple. *Phys. Rev. Lett.* **77**, 3865-3868 (1996).
84 Grimme, S., Antony, J., Ehrlich, S. & Krieg, H. A Consistent and Accurate Ab Initio Parametrization of Density Functional Dispersion Correction (DFT-D) for the 94 Elements H-Pu. *J. Chem. Phys.* **132**, 154104 (2010).
85 Livraghi, S., Paganini, M. C., Giamello, E., Di Liberto, G., Tosoni, S. & Pacchioni, G. Formation of Reversible Adducts by Adsorption of Oxygen on Ce–ZrO_2: An Unusual η^2 Ionic Superoxide. *J. Phys. Chem. C* **123**, 27088-27096 (2019).
86 Monkhorst, H. J. & Pack, J. D. Special Points for Brillouin-Zone Integrations. *Phys. Rev. B* **13**, 5188-5192 (1976).
87 Makov, G. & Payne, M. C. Periodic Boundary Conditions in Ab Initio Calculations. *Phys. Rev. B* **51**, 4014-4022 (1995).
88 Harris, J. Simplified Method for Calculating the Energy of Weakly Interacting Fragments. *Phys. Rev. B* **31**, 1770-1779 (1985).
89 Henkelman, G., Uberuaga, B. P. & Jónsson, H. A Climbing Image Nudged Elastic Band Method for Finding Saddle Points and Minimum Energy Paths. *J. Chem. Phys.* **113**, 9901-9904 (2000).

90 Henkelman, G. & Jónsson, H. Improved Tangent Estimate in the Nudged Elastic Band Method for Finding Minimum Energy Paths and Saddle Points. *J. Chem. Phys.* **113**, 9978-9985 (2000).
91 Sheppard, D., Terrell, R. & Henkelman, G. Optimization Methods for Finding Minimum Energy Paths. *J. Chem. Phys.* **128**, 134106 (2008).
92 Heyden, A., Bell, A. T. & Keil, F. J. Efficient Methods for Finding Transition States in Chemical Reactions: Comparison of Improved Dimer Method and Partitioned Rational Function Optimization Method. *J. Chem. Phys.* **123**, 224101 (2005).
93 Olsen, R. A., Kroes, G. J., Henkelman, G., Arnaldsson, A. & Jónsson, H. Comparison of Methods for Finding Saddle Points Without Knowledge of the Final States. *J. Chem. Phys.* **121**, 9776-9792 (2004).
94 Pechukas, P. Transition State Theory. *Annu. Rev. Phys. Chem.* **32**, 159-177 (1981).
95 Haworth, N. L., Wang, Q. & Coote, M. L. Modeling Flexible Molecules in Solution: A pKa Case Study. *J. Phys. Chem. A* **121**, 5217-5225 (2017).
96 Campbell, C. T. & Sellers, J. R. V. The Entropies of Adsorbed Molecules. *J. Am. Chem. Soc.* **134**, 18109-18115 (2012).
97 Shampine, L. F. & Reichelt, M. W. The MATLAB ODE Suite. *SIAM J. Sci. Comput.* **18**, 1-22 (1997).
98 Shampine, L. F., Reichelt, M. W. & Kierzenka, J. A. Solving Index-1 DAEs in MATLAB and Simulink. *SIAM Rev.* **41**, 538-552 (1999).
99 You, K.-E., Ammal, S. C., Lin, Z. & Heyden, A. Understanding Selective Hydrodeoxygenation of 1,2- and 1,3-Propanediols on Cu/Mo_2C via Multiscale Modeling. *ACS Catal.* **12**, 4581-4596 (2022).
100 Zhao, E. W., Maligal-Ganesh, R., Xiao, C., Goh, T.-W., Qi, Z., Pei, Y. *et al.* Silica-Encapsulated Pt-Sn Intermetallic Nanoparticles: A Robust Catalytic Platform for Parahydrogen-Induced Polarization of Gases and Liquids. *Angew. Chem. Int. Ed.* **56**, 3925-3929 (2017).
101 Bowers, C. R. Sensitivity Enhancement Utilizing Parahydrogen. *eMagRes* (2007).